https://doi.org/10.5194/egusphere-2025-5714
Preprint. Discussion started: 19 December 2025

The role of structural heterogeneity in glacier ice deformation: Insights from Planpincieux Glacier

Thomas Chauve[1], Florent Gimbert[1], Adrien Gilbert[1], Olivier Gagliardini[1], Luc Piard[1], Arnaud Reboud[1], Olivier Laarman[1], Paolo Perret[2,4], William Boffelli[2], Pietro Di Sopra[2], Luca Mondardini[2,3], and Fabrizio Troilo[2]

[1]Univ. Grenoble Alpes, CNRS, INRAE, IRD, Grenoble INP, IGE, 38000 Grenoble, France
[2]Fondazione Montagna sicura - Montagne sûre, Courmayeur, 11013, Italy
[3]Dept. of Computer Science "Giovanni degli Antoni", University of Milano, Via Celoria 18, 20133 Milano, Italy
[4]Dept. of Electrical, Computer Science and Biomedical Engineering, University of Pavia, Via Ferrata 1, 27100 Pavia, Italy

Correspondence: Thomas Chauve (thomas.chauve@univ-grenoble-alpes.fr)

Abstract. Natural glacier ice is not a monophasic, isotropic material as commonly assumed in models based on Glen-Nye's flow law. It can contain crevasses, develop crystallographic preferred orientations, and include mixtures of debris and interstitial water in temperate glaciers. Understanding the influence of such structural heterogeneities on deformation is therefore essential for accurately modeling glacier dynamics. In this study, we investigate the multi-scale evolution of structural heterogeneities with depth in the Planpincieux Glacier (Italian Mont Blanc massif) and evaluate their respective influence on ice deformation using a borehole instrumented with an optical televiewer, a full-waveform sonic logger, a piezometer, and an inclinometer chain. Complementary GNSS and seismic data provide additional constraints on hydrological activity and surface motion. Optical and sonic logging reveal two main families of heterogeneities: open and closed crevasses in the upper 60 m, and debris-rich layers near the bedrock interface. Acoustic data show continuous but opposite trends in both P- and Stoneley-wave velocities with depth, interpreted as reflecting an increase in water content but a decrease in permeability. Tiltmeter measurements indicate that roughly one-third of the surface velocity is accommodated by internal deformation, with pronounced strain localization near the bedrock, particularly within debris-rich layers. These layers exhibit enhanced strain following hydrological drainage events, suggesting a coupling between mechanical heterogeneity, basal hydrology, and strain localization. The results highlight that glacier friction laws may be significantly influenced by such heterogeneities, including the effects of interstitial water and debris on local mechanical behavior.

1 Introduction

The Glen-Nye flow law (Nye, 1953; Glen, 1955), commonly used in numerical glacier modeling, treats glacier ice as a single-phase, isotropic material whose fluidity depends solely on temperature (Cuffey and Paterson, 2010), and relates stress to strain rate through a non-linear power-law relationship, typically with an exponent of $n = 3$ (Duval et al., 1983). These assumptions, however, overlook the complexity of natural ice, which is known to develop heterogeneities of various origins.

https://doi.org/10.5194/egusphere-2025-5714
Preprint. Discussion started: 19 December 2025

A first source of heterogeneity is anisotropy, expressed through the development of crystallographic preferred orientations (CPO), as evidenced by ice-core analyses in ice sheets (e.g. Lipenkov et al., 1989; Thorsteinsson et al., 1997; Azuma et al., 1999; Durand et al., 2009; Montagnat et al., 2014; Stoll et al., 2024) and mountain glaciers (Rigsby, 1960; Tison and Hubbard, 2000; Gerbi et al., 2021; Hellmann et al., 2021; Monz et al., 2021). Such strong CPOs induce significant mechanical anisotropy, potentially altering the bulk fluidity of ice by more than one order of magnitude (Jacka and Maccagnan, 1984; Jacka and Budd, 1989; Treverrow et al., 2012; Montagnat et al., 2015; Qi et al., 2017; **?**). A second source of heterogeneity arises from the coexistence of ice with other phases. In temperate glaciers, liquid water can persist at the pressure-melting point, either by maintaining crevasse openings at depth (Hubbard et al., 2021) or as interstitial inclusions within the ice matrix (De La Chapelle et al., 1999). Interstitial water contents ranging from 0.5 % to 2 % have been measured in alpine glaciers (Vallon et al., 1976; Lliboutry and Duval, 1985; Lüthi et al., 2025) and have been shown to enhance ice fluidity (Duval, 1977; Adams et al., 2021), following a linear flow behavior with an effective stress exponent of $n = 1$ (Newtonian fluid) (Schohn et al., 2025). Finally, natural ice can contain additional solid phases, such as impurities that influence both microstructural development and CPO evolution (Durand et al., 2006), or mixtures of ice and rock debris identified through structural glaciological observations (Hudleston, 2015; Jennings and Hambrey, 2021) and borehole optical logging (Hubbard et al., 2008; Miles et al., 2021). The influence of these heterogeneities on ice rheology remains complex and not yet fully understood (Moore, 2014).

Quantifying heterogeneity in the vicinity of glaciers remains a challenging task, as structural observations are often restricted to exposed outcrops (Hudleston, 2015; Jennings and Hambrey, 2021). Ice-core drilling allows detailed crystallographic and impurity characterization with depth, but such studies are typically conducted at sites with low strain rates and stable flow, where climatic signal preservation is prioritized (Lipenkov et al., 1989; Thorsteinsson et al., 1997; Azuma et al., 1999; Durand et al., 2009; Montagnat et al., 2014). Other techniques based on the measurement of elastic wave propagation have been used to infer the evolution of CPO with depth. Because of the intrinsic elastic anisotropy of ice single crystals, wave velocities are sensitive to the bulk anisotropy of polycrystalline ice (Maurel et al., 2016; Rathmann et al., 2022). Sonic logging (Gusmeroli et al., 2012; Kluskiewicz et al., 2017; Lutz et al., 2022) and distributed acoustic sensing (Booth et al., 2020) have been employed to estimate variations in elastic wave velocities with depth, and have so far been deployed mainly in cold glaciers. Optical borehole logging has also been used to characterize glacier structures. Hubbard et al. (2021) observed crevasses down to 400 m depth in a 900 m borehole, showing multiple cycles of opening and refreezing. Such deformation mechanisms have been suggested to locally warm the ice through the release of latent heat during refreezing. Other optical observations revealed increasing debris concentration with depth, although debris remains heterogeneously distributed in discrete, dense layers (Miles et al., 2021). Investigations focusing on water content in temperate glaciers are, to our knowledge, limited. Vallon et al. (1976) measured water content along an ice core drilled in the French Alps using calorimetry, reporting an increase with depth from 0 to 2% and suggesting shear heating as a mechanism for liquid water production. More recently, Lüthi et al. (2025) performed calorimetric measurements in basal cavities of two temperate glaciers, providing local basal-ice water content estimates between 1 and 2%.

Although estimating heterogeneity remains complex, linking these structural features to deformation processes near glacier beds is even less well understood, limiting our ability to accurately model glacier dynamics. Strain rate measurements using englacial tiltmeters (Gudmundsson et al., 1999; Willis et al., 2003; Amundson et al., 2006; Ryser, Claudia, 2014; Keller and

https://doi.org/10.5194/egusphere-2025-5714
Preprint. Discussion started: 19 December 2025

Blatter, 2012; Doyle et al., 2018; Lee et al., 2019; Maier et al., 2019, 2021; Roldán-Blasco et al., 2024) have shown significant vertical variability, which could not be reproduced by models assuming spatially homogeneous fluidity (Derkacheva et al., 2021; Roldán-Blasco et al., 2024), regardless of the stress exponent applied. Instead, ad hoc spatial variations in fluidity were required to match the observations (Roldán-Blasco et al., 2024). Lüthi et al. (2002) reported enhanced deformation in Wisconsin-age ice correlated with elevated dust concentrations. Although the underlying mechanical link was not fully resolved, it is likely that preferential CPO development may play a role, as dust is known to promote recrystallization processes (Duval and Lorius, 1980; Thorsteinsson et al., 1997). More recently, seismic observations at the EastGRIP borehole in Greenland revealed cascades of microseismic events nucleating near impurity-rich layers (Fichtner et al., 2025). These events are interpreted as deformation bursts localized within impurity-bearing strata, further emphasizing the potential role of structural heterogeneity in driving localized deformation. However, the fraction of the total deformation accommodated by these layers remains unknown.

In this study, we investigate the relationship between deformation, measured using englacial tiltmeters, and structural heterogeneity, characterized through optical and sonic logging within a borehole in the Planpincieux Glacier, located in the Mont Blanc massif.

2 Methodology

2.1 Field site: Planpincieux Glacier

The Planpincieux Glacier is a polythermal glacier located on the Italian side of the Mont Blanc massif (45.85°N, 6.97°E), with an elevation range from 2530 m to 3700 m a.s.l. (Fig. 1(a)). The glacier is monitored by the *Fondazione Montagna Sicura*, as it poses a potential hazard to the village of Planpincieux in the *Val Ferret* valley (Giordan et al., 2020; Dematteis et al., 2017, 2021, 2024).

During the summer of 2024, a field campaign was carried out on the plateau above the serac fall at the glacier terminus, between 2900 and 3000 m a.s.l. One borehole was drilled using a custom-built hot-water drill. A piezometer was installed at the ice–bedrock interface, and a tiltmeter chain was deployed within the borehole, recording measurements every 10 minutes. A GPS antenna was placed next to the borehole, with a reference station established at the Boccalatte hut, approximately 500 m away. In addition, a broadband seismic sensor (0.1–98 Hz, red) was deployed on the glacier, and two narrower-band sensors (4.5–98 Hz, blue) were installed on the left and right banks of the torrents draining the glacier, recording signals at 200 Hz. The deployment layout is shown in Fig. 1(a).

This borehole was first instrumented with optical and sonic logging tools, prior to the installation of the piezometer and tiltmeter chain, in order to investigate the structural heterogeneities of the glacier.

Additional topographic datasets are available for the Planpincieux Glacier, including a surface digital elevation model (DEM) acquired by drone on 9 July 2024, a bedrock DEM derived from ground-penetrating radar, and mean annual surface velocities for the period 2015–2021 obtained from satellite imagery produced by Rabatel et al. (2023). Figures 1(b,c) show the bedrock topography and a cross-section along a flowline extracted from the 2021 velocity field. The topography reveals a central

https://doi.org/10.5194/egusphere-2025-5714
Preprint. Discussion started: 19 December 2025

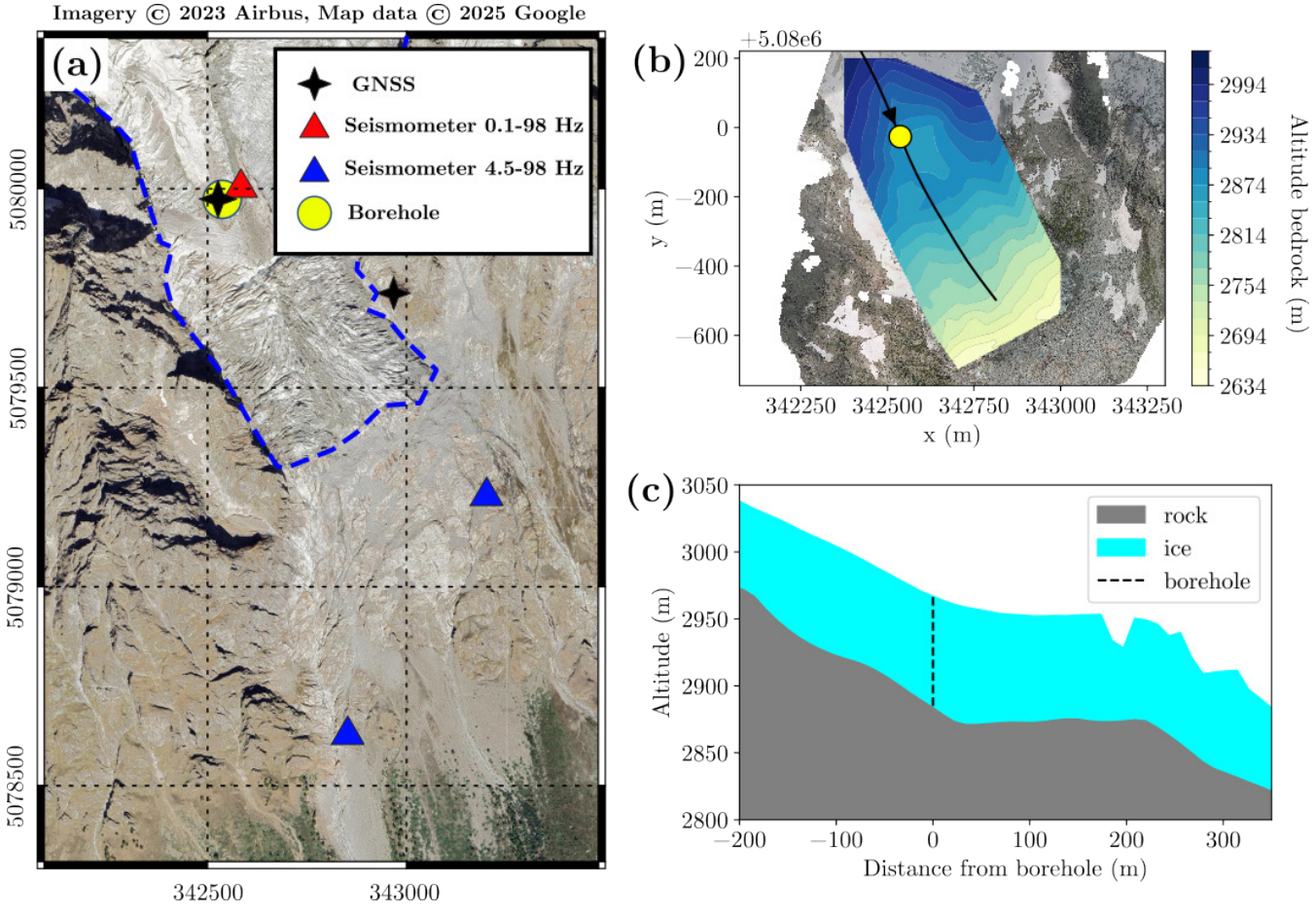

Figure 1. *(a)* Planpincieux Glacier map showing the instrumentation deployment (©Imagery © 2023 Airbus, Map data © 2025 Google). The dashed blue line shows the boundary of Planpincieux Glacier. The black stars indicate GNSS stations installed on the glacier and the associated GNSS base near the Boccalatte hut. The triangle marks the location of the seismometers: one broadband sensor (0.1–98 Hz, red) on the glacier, and two narrower-band sensors (4.5–98 Hz, blue) on the left and right banks of the torrents draining the glacier. The yellow dot denotes the position of the hot-water–drilled borehole, instrumented with an inclinometer chain and a piezometer. All positions on the glacier correspond to 20 August 2024 (EPSG:32632). *(b)* Bedrock topography of the Planpincieux Glacier. The yellow dot marks the position of the borehole on 20 August 2024. The black line indicates the streamline passing through the borehole, computed from surface velocity data measured by satellite imagery from Rabatel et al. (2023) (EPSG:32632). *(c)* Cross section of the bedrock topography along the streamline passing through the borehole. The surface topography was acquired by optical stereography on 9 July 2024.

https://doi.org/10.5194/egusphere-2025-5714
Preprint. Discussion started: 19 December 2025

depression located downstream of the borehole site, approximately 200 m upstream of the slope break that marks the beginning of the serac fall at the glacier terminus.

2.2 Field instruments

2.2.1 Optical logging

A *QL40-OBI* optical televiewer from *Mount Sopris Instruments* was used to perform optical stratigraphy of the borehole wall. This tool provides a geographically oriented RGB image of the borehole's lateral surface. Two logging runs were conducted, both performed from bottom to top in order to maximize the probe stability: the first immediately after drilling, covering depths from 4 m to 94 m, and the second 16 hours later, covering the interval from 90 m to 97 m. Figure B1 presents the RGB images from both measurements at overlapping depths (92 to 94 m). At this depth, the images reveal granite debris incorporated within the ice, with particle sizes reaching up to the centimeter scale. The comparison between the two logs also highlights the benefit of waiting before performing the optical scan, as suspended particles have time to settle, resulting in a clearer image. This decantation period is particularly valuable when debris is embedded within the ice matrix, as it enhances the visibility of structural features.

To ensure accurate scaling of the borehole images, the borehole diameter was measured using a mechanical caliper (*QL40-CAL* 3-Arm Caliper). The average diameter recorded between 92 and 94 m depth was 135 mm, corresponding to a perimeter of 42.4 cm. This measurement allowed the images to be displayed with the correct aspect ratio, providing a realistic representation of the borehole wall geometry. Additionally, the caliper data enabled the extraction of the orientation of planes intersecting the cylindrical borehole. The intersection of a planar feature with the cylindrical surface produces a sinusoidal trace on the unwrapped image (Fig. 3), from which the planes were manually extracted.

2.2.2 Sonic logging

A *QL40-FWS* sonic logger from *Mount Sopris Instruments* was used to measure the propagation of acoustic waves within the ice. The *QL40-FWS* is equipped with a single acoustic source, a monopole transducer with a 15 kHz resonant frequency, and four receivers positioned at intervals of 20 cm, ranging from 60 cm to 120 cm from the source.

Figure 2 illustrates the different modes of wave propagation occurring during borehole logging: two body waves (P-waves and S-waves) and one interface wave (Stoneley-waves).

The P- and S-waves sample the ice surrounding the borehole. P-waves propagate with particle motion parallel to the propagation direction, whereas S-waves propagate with particle motion perpendicular to it (Fig. 2(a-b)). The velocities of these waves can be used to estimate the elastic anisotropy of ice, which is related to the crystallographic preferred orientation (CPO) (Gusmeroli et al., 2012; Maurel et al., 2016; Kluskiewicz et al., 2017). At 0°C, P-wave velocities range from 3726 m s^{-1} for uniform CPO to 3906 m s^{-1} for a single-maximum CPO along the single maximum direction, while S-wave velocities range from 1900 m s^{-1} to 1746 m s^{-1} over the same CPO range. For an isotropic material, the P-wave velocity depends on the bulk modulus K, the shear modulus G, and the material density ρ, according to (Aki and Richards, 2002)

https://doi.org/10.5194/egusphere-2025-5714
Preprint. Discussion started: 19 December 2025

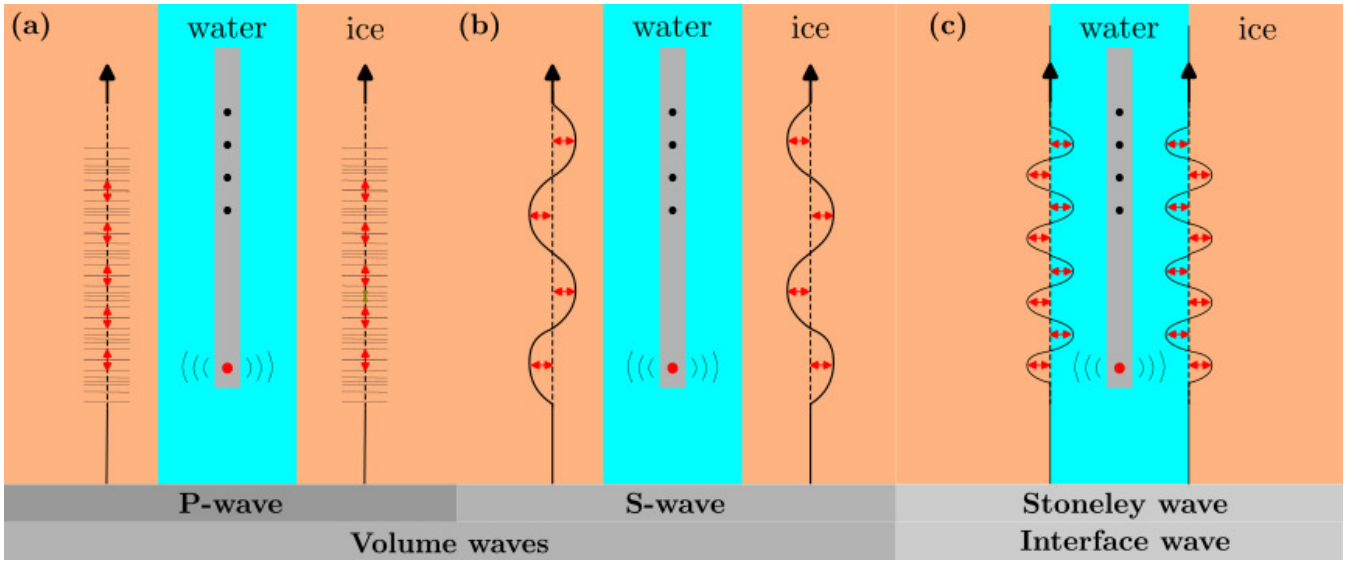

Figure 2. Schematic representation of wave propagation during borehole logging. *(a)* P-wave propagation with particle motion (red arrows) parallel to the propagation direction. *(b)* S-wave propagation with particle motion (red arrows) perpendicular to the propagation direction. *(c)* Stoneley-wave propagation at the borehole interface, with particle motion (red arrows) perpendicular to the propagation direction.

$$Vp = \sqrt{\frac{K_{ice} + \frac{4}{3}G_{ice}}{\rho_{ice}}}. \tag{1}$$

Stoneley-waves propagate along the fluid–solid interface with particle motion perpendicular to the propagation direction (Fig. 2(c)). These waves generate a pressure differential at the interface, pumping fluid in and out of the medium, which results in attenuation and a reduction in Stoneley-wave velocity. Variations in Stoneley-wave velocity are therefore commonly interpreted, particularly in petrophysical applications, as indicators of microfracturing and permeability (Saxena et al., 2018; Mari et al., 2020). A first-order approximation of the Stoneley-wave velocity C_{St} is given by White's model, which relates it to the fluid density ρ_f, the bulk modulus of the fluid K_{bf}, and the shear modulus of the borehole wall G (White, 1983; Saxena et al., 2018):

$$C_{St} = \left[\rho_{water}\left(\frac{1}{K_{water}} + \frac{1}{G_{ice}}\right)\right]^{-\frac{1}{2}}. \tag{2}$$

Using the values measured by Gammon et al. (1983) at -16°C, $K_{ice} = 8.9{\times}10^9\ Pa$, $G_{ice} = 3.52{\times}10^9\ Pa$, $\rho_{ice} = 917\ kg.m^{-3}$, $K_{water} = 1.96{\times}10^9\ Pa$, and $\rho_{water} = 1000\ kg.m^{-3}$, we obtain a P-wave velocity of 3800 m s^{-1} and a Stoneley-wave velocity of about 1120 m s^{-1}.

https://doi.org/10.5194/egusphere-2025-5714
Preprint. Discussion started: 19 December 2025

2.2.2.a Picking arrival time

The arrival time of the P-waves was determined by selecting the zero-crossing of the waveform immediately following the initial local maximum in the recorded pressure signal for each receiver, following the approach of Kluskiewicz et al. (2017). The P-wave velocity (V_p) was then calculated by performing a linear regression of these arrival times as a function of receiver distance and subsequently smoothed using a rolling average over 20 measurements. The same procedure was applied to extract the acoustic absorption coefficient α, which characterizes the exponential decay of the maximum signal amplitude with propagation distance, according to the relation $A(z) = \exp(-\alpha z)$.

2.2.2.b Semblance analysis

Semblance analysis, which is commonly used in petrophysics (Akhmetsafin et al., 2008; Mari et al., 2020), computes, for each given time t along the signal over a fixed time window wt, the correlation between M measured signals f_m recorded at the position z_m along the probe, assuming a shift corresponding to a constant wave propagation velocity v over the probe length, as expressed by the equation 3:

$$\mathrm{Semb}(t,v) = \frac{\int_t^{t+\mathrm{wt}} \left\{ \sum_{m=1}^{M} f_m\left(\frac{z_m}{v} + \tau\right) \right\}^2 d\tau}{\int_t^{t+\mathrm{wt}} \sum_{m=1}^{M} f_m^2\left(\frac{z_m}{v} + \tau\right) d\tau}. \quad (3)$$

This semblance value evolves between 0 (no correlation) and 1 (perfect correlation) enables detection the arrival of different waves propagating at different velocity.

Wave velocities were then determined by averaging the semblance over a given time and velocity window, and by selecting the velocity corresponding to the maximum semblance value. Compared to arrival time picking, semblance analysis has the advantage of enabling the detection of multiple wave types within the signal, whereas the time-of-arrival method is limited to the first arrival, corresponding to the P-waves.

2.2.3 Tiltmeter chain

The same type of tiltmeter chain as used in Roldán-Blasco et al. (2024) was deployed in the borehole, recording inclination relative to the vertical using triaxial gravity sensors (SCL3300, Murata) at 10-minute intervals, with an estimated accuracy of $0.01°$. The chain consists of 15 tiltmeters, with a higher sensor density toward the base of the glacier, where stronger deformation is expected. Mechanical coupling between the tiltmeters and the surrounding ice is achieved through borehole closure driven by ice deformation, as no refreezing is expected in the temperate ice. The rate of closure depends on local stress conditions and the presence of water within the borehole. The date at which all tiltmeters are considered to be mechanically coupled is 17 September 2024, as indicated by a marked decrease in angle measurement variability (Fig. D1).

The reference frame is defined with the x-axis aligned with the glacier flow direction and the z-axis oriented vertically downward, originating at the glacier surface. Velocities in the x, y, and z directions are denoted by u, v, and w, respectively.

https://doi.org/10.5194/egusphere-2025-5714
Preprint. Discussion started: 19 December 2025

Following Roldán-Blasco et al. (2024), we assume that the evolution of the tilt angle θ is dominated by the shear strain $\frac{du}{dz}$, which can be approximated as:

$$\frac{du}{dz} = \frac{1}{dt}\frac{dx}{dz} \simeq \frac{1}{\Delta t}\Delta\tan(\theta) \tag{4}$$

To increase the signal-to-noise ratio, we apply a rolling average over a 6-hour window, denoted as $\langle\cdot\rangle_{6h}$:

$$\left\langle \frac{du}{dz} \right\rangle_{6h} \simeq \left\langle \frac{1}{\Delta t}\Delta\tan\left(\langle\theta\rangle_{6h}\right) \right\rangle_{6h} \tag{5}$$

2.2.4 Stress and fluidity estimation

To estimate ice fluidity from the strain rates measured by the inclinometer chain, it is first necessary to determine the stress field. For this purpose, we follow the same approach as Roldán-Blasco et al. (2024).

The stress components τ_{ij} and strain rate components $\dot{\varepsilon}_{ij}$ are related through Glen-Nye's flow law (Glen, 1955) via the fluidity parameter A, according to :

$$\dot{\varepsilon}_{ij} = A\tau_e^{n-1}\tau_{ij}, \tag{6}$$

with $\tau_e = \sqrt{\frac{1}{2}\tau_{ij}\tau_{ij}}$.

Therefore, estimating the stress along the borehole allows the fluidity to be determined. Two approaches are used to compute the stress.

The first approach employs a simplified Shallow Ice Approximation (SIA) assuming plane-strain. In this framework, the only non-zero component of the stress tensor, τ_{xz}, at a given depth z, depends on the weight of the overlying ice column and on the surface slope α, such as:

$$\tau_{xz} = \rho g z \times sin(\alpha), \tag{7}$$

with ρ the ice density and g the gravitational acceleration.

Using the SIA formulation tends to overestimate the shear stress, as no lateral drag is considered to counterbalance the ice flow (Nye, 1965; Roldán-Blasco et al., 2024). Therefore, a geometrical shape factor f can be introduced in order to reduce the shear stress, also named fSIA:

$$\tau_{xz} = f\rho g z \times \sin(\alpha). \tag{8}$$

Nye (1965) provides shape factor tabulation as a function of bedrock geometry and the glacier aspect ratio W.

https://doi.org/10.5194/egusphere-2025-5714
Preprint. Discussion started: 19 December 2025

The second, more advanced approach consists of using the three-dimensional, full-Stokes finite-element model Elmer/Ice (Gagliardini et al., 2013) to solve the conservation of momentum for a prescribed glacier geometry and ice rheology. Details of the model implementation are provided in Roldán-Blasco et al. (2024). The resulting simulation yields all components of the three-dimensional stress tensor, which can subsequently be used to estimate the fluidity A.

3 Results

3.1 Structural heterogeneity of glacier ice revealed by optical and acoustic logging

3.1.1 Overview from optical log

The optical logger, also referred to as OPTV imaging, enables visualization of the borehole wall and its stratigraphy. Figure 3 presents four distinct types of features observed at depth, along with the corresponding orientations of their planes.

The dominant features are dust foliation planes, which are observed throughout the borehole (Fig. 3(a)). The orientation of these planes, shown in the stereographic projection of Fig. 3(a), forms a cluster near the west direction at depths of around 50 m, progressively rotating toward the southeast with increasing depth. This trend tends to align with the orientation of the surface slope at the drilling site (blue square, Fig. 3(a)).

The second type of feature consists of open crevasses. Four open crevasses are visible in the optical stratigraphy down to 53 m depth (Figs. B2, 5). No distinct clustering of crevasse-plane orientations is apparent in the stereographic projection due to the limited number of observations (Fig. 3(b)). The presence of these crevasses is also confirmed by the caliper data, which display a characteristic profile when crossing a crevasse, marked by a sharp discontinuity at the lower contact and a smoother transition at the upper contact (Appendix C).

The third type of feature corresponds to closed crevasses. These appear as white, sinusoidal traces along the borehole wall (Figs. 3(c) and 6). Such traces are interpreted by Hubbard et al. (2021) as air bubbles trapped during the refreezing of previously open crevasses. These structures cluster toward the southeast direction and are primarily located between depths of 30 and 50 m.

Finally, near the bedrock interface, at 97.5 m depth, a high concentration of granite debris is visible in the optical stratigraphy. Debris clasts reach sizes of several centimeters between 92.25 m and 94.75 m depth, forming debris-rich layers at 92.75 m, 93.75 m, and 94.6 m, about 0.5 to 1 m thick, interspersed with less concentrated layers at 93.4 m and 94.25 m (Fig. 7(d)). The orientations of these debris layers cluster around a direction close to that of the surface slope (Fig. 3(d)).

3.1.2 Links with sonic log

3.1.2.a Semblance analysis

Figure 4 shows, for a given set of recorded signals at 57 m depth (Fig. 4(a)), the semblance function computed for velocities between 930 and 5000 m s^{-1} (Fig. 4(b)). The first high-correlation peak near 3800 m s^{-1} corresponds to the P-wave arrival (Fig. 4(b), V_p dashed box), and the second peak near 1100 m s^{-1} corresponds to the Stoneley-wave arrival (Fig. 4(b),

https://doi.org/10.5194/egusphere-2025-5714
Preprint. Discussion started: 19 December 2025

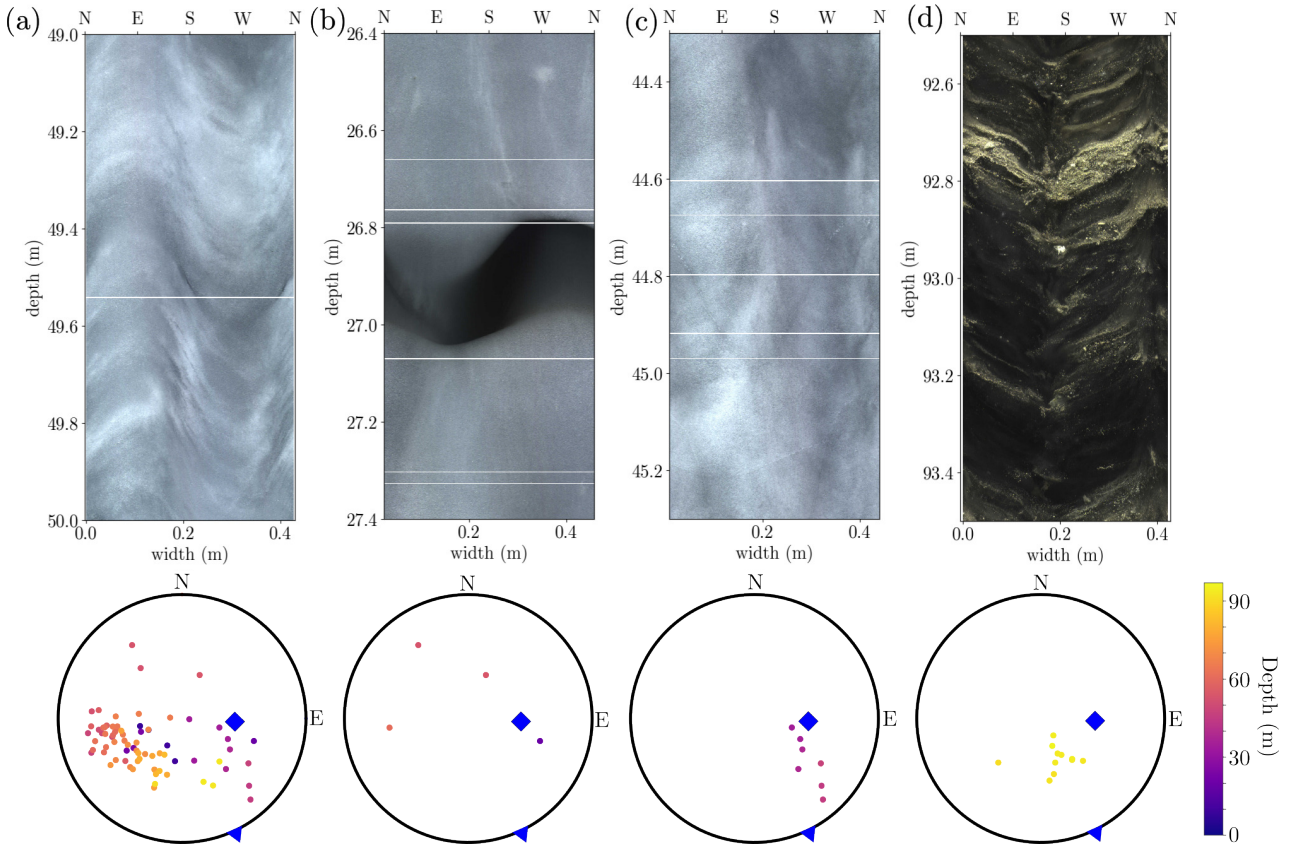

Figure 3. Variety of structural heterogeneities observed along the optical logs. *(a)* Dust layering, *(b)* open crevasses, *(c)* closed crevasses, and *(d)* debris-rich layers. The stereographic projection displays the orientations of the plane normals over the complete log, color-coded by depth from 0 to 97 m. The blue square indicates the normal to the glacier surface, and the blue triangle marks the flow-direction vector at the borehole location. The white lines in the optical images are missing data due to buffer overload during logging.

V_{St} dashed box). The P-wave and Stoneley-wave velocities are computed by averaging the signal in each delimited box and selecting the velocity with maximum average semblance (Fig. 4(d-e)).

At 57 m depth, semblance analysis allows the extraction of both P-waves and Stoneley-waves with good confidence, as the average semblance reaches values up to 0.75. Another example is shown at 53 m depth, where the probe receivers intersect an open crevasse filled with liquid water (Fig. A1). In this case, the propagation velocity is not expected to remain constant ($V_{p,\mathrm{ice}} \sim 3800$ m s^{-1}, $V_{p,\mathrm{water}} \sim 1500$ m s^{-1}). Consequently, the correlation performed under the assumption of a constant velocity shift results in low semblance values (< 0.3). For this reason, the average semblance value is subsequently used as a quality criterion to discard measurements with low confidence (average semblance < 0.5).

No clear S-waves are visible in the semblance analysis and are therefore not discussed further (Figs. 4, A1).

https://doi.org/10.5194/egusphere-2025-5714
Preprint. Discussion started: 19 December 2025

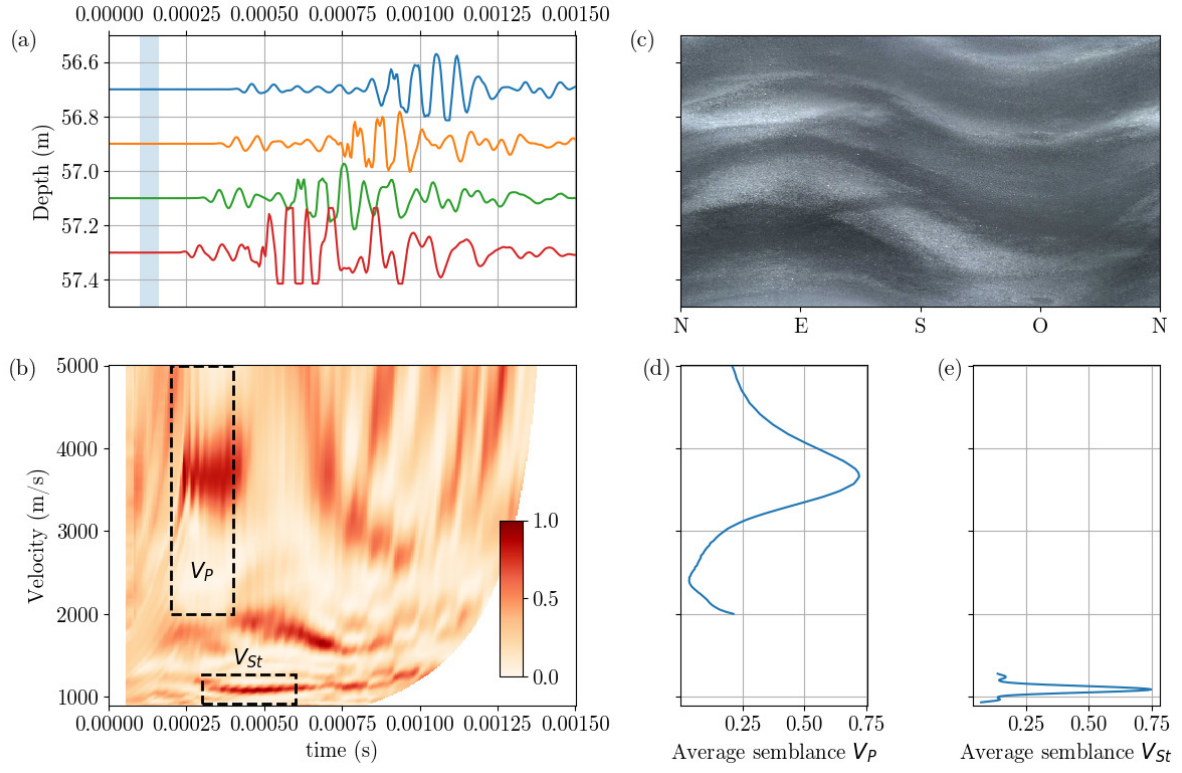

Figure 4. *(a)* Four recorded signals by the sonic logger at 57 m depth. The vertical blue-shaded area shows the length of the wt parameter used in the semblance analysis (Eq. 3). *(b)* The semblance analysis for velocities ranging from 930 to 5000 m s^{-1}. The dashed rectangles show the function range used to determine the P-wave velocity and the Stoneley-wave velocity by taking the maximum of the average semblance over this range *(d)* and *(e)*. *(c)* Optical image recorded by the optical logger at the same depth.

225 The comparison between P-wave velocities derived from arrival time and semblance are consistent, provided that the sampled volume is homogeneous (Fig. 5 between 51.5 and 52.5 m).

Figure 5 presents a 3 m section between 51.5 and 54.5 m depth where an open crevasse is visible in both the caliper log and the optical image (Figs. 5(a,d)). In this case, the semblance analysis does not provide a reliable P-wave velocity estimate (Figs. 5(c) and A1), whereas the time-of-arrival method still yields a measurement. This is because the linear regression
230 averages out the heterogeneity of P-wave velocities within the sampled volume. As a result, crevasses can be detected even when they are not clearly visible in the optical imagery (Figs. 5 and 6). Therefore, the two approaches are complementary.

https://doi.org/10.5194/egusphere-2025-5714
Preprint. Discussion started: 19 December 2025

3.1.2.b Impact of the features on wave propagation

Dust foliation planes are the dominant features observed along the borehole, as illustrated in Fig. 3(a). These planes are characterized by low acoustic absorption and a relatively homogeneous P-wave velocity of approximately 3750 $\mathrm{m\,s^{-1}}$, as measured by the sonic logger using both the time-of-arrival and semblance analyses (Fig. 5 between 51.5 and 52.5 m).

When the acoustic probe crosses an open crevasse, the P-wave velocity measured using the time-of-arrival technique decreases with increasing crevasse width: 3420 $\mathrm{m\,s^{-1}}$ for the 25 cm-wide crevasse and 2718 $\mathrm{m\,s^{-1}}$ for the 50 cm-wide crevasse. The semblance analysis simultaneously reveals a loss of correlation (Figs. B2(c), 5(c)). In parallel, the presence of crevasses increases acoustic absorption, with values reaching up to 5 $\mathrm{m^{-1}}$ (Figs. B2(b), 5(b)). Above the crevasse, the P-wave velocity increases to about 4200 $\mathrm{m\,s^{-1}}$, although no corresponding heterogeneity is visible in the optical imagery (Fig. 5).

Closed crevasses exhibit variable acoustic behavior depending on their proximity to either dust layers or open crevasse structures. The closed crevasse at 45 m depth shows P-wave velocities and acoustic absorption similar to those measured in clean ice containing only dust layers (Fig. B4). In contrast, the crevasse at 38 m depth (Fig. 6) displays characteristics comparable to those of open crevasses (e.g., Fig. 5), including an increased borehole diameter, elevated acoustic absorption, and reduced P-wave velocity, overlain by a layer of higher velocity. It is therefore likely that the crevasse observed at 38 m depth represents the tip of a larger fracture. This would explain why the optical image suggests a closed crevasse, whereas the velocity measurements—which sample a larger volume of ice beyond the borehole walls—still reveal a pronounced reduction in P-wave velocity.

Finally, the presence of debris also affects sonic wave propagation, leading to lower P-wave velocities and significantly higher acoustic absorption (Fig. 7(b,c)).

3.1.2.c Wave-velocity trends with depth

The depth profiles of Stoneley-wave and P-wave velocities estimated from semblance analysis are shown in Fig. 8(a,b). The analysis focuses on the interval between 57 and 90 m depth in order to avoid the influence of open crevasses observed down to 53 m depth (Fig. 5). In this depth range, it is worth noting that the borehole diameter exhibits a non-significant negative trend with depth of -0.09 $\mathrm{mm\ m^{-1}}$ (Fig. C2).

The Stoneley-wave velocity has an average value of 1098 $\mathrm{m\ s^{-1}}$, with an increasing trend with depth of $+0.55$ $\mathrm{m\ s^{-1}.m^{-1}}$. This range of velocities is consistent with the prediction of White's model (1115 $\mathrm{m\ s^{-1}}$). The trend results in a shift of the Stoneley-wave velocity from 1104 $\mathrm{m\ s^{-1}}$ in the upper interval (57–68 m depth) to 1093 $\mathrm{m\ s^{-1}}$ in the deeper interval (79–90 m depth) (Fig. 8(a)).

Over the same depth range, the P-wave velocity exhibits an average value of 3615 $\mathrm{m\ s^{-1}}$, which is lower than the theoretical velocity for polycrystalline ice with either a uniform texture (3726 $\mathrm{m\ s^{-1}}$) or a single maximum CPO aligned with the borehole direction (3906 $\mathrm{m\ s^{-1}}$) (Kluskiewicz et al., 2017). The P-wave velocity decreases with depth at a rate of -2 $\mathrm{m\ s^{-1}.m^{-1}}$, shifting from an average value of 3640 $\mathrm{m\ s^{-1}}$ between 57–68 m depth to 3581 $\mathrm{m\ s^{-1}}$ between 79–90 m depth (Fig. 8(b)).

These observations reveal two opposite trends in Stoneley- and P-wave velocities with depth, which are likely linked to heterogeneities in the ice.

https://doi.org/10.5194/egusphere-2025-5714
Preprint. Discussion started: 19 December 2025

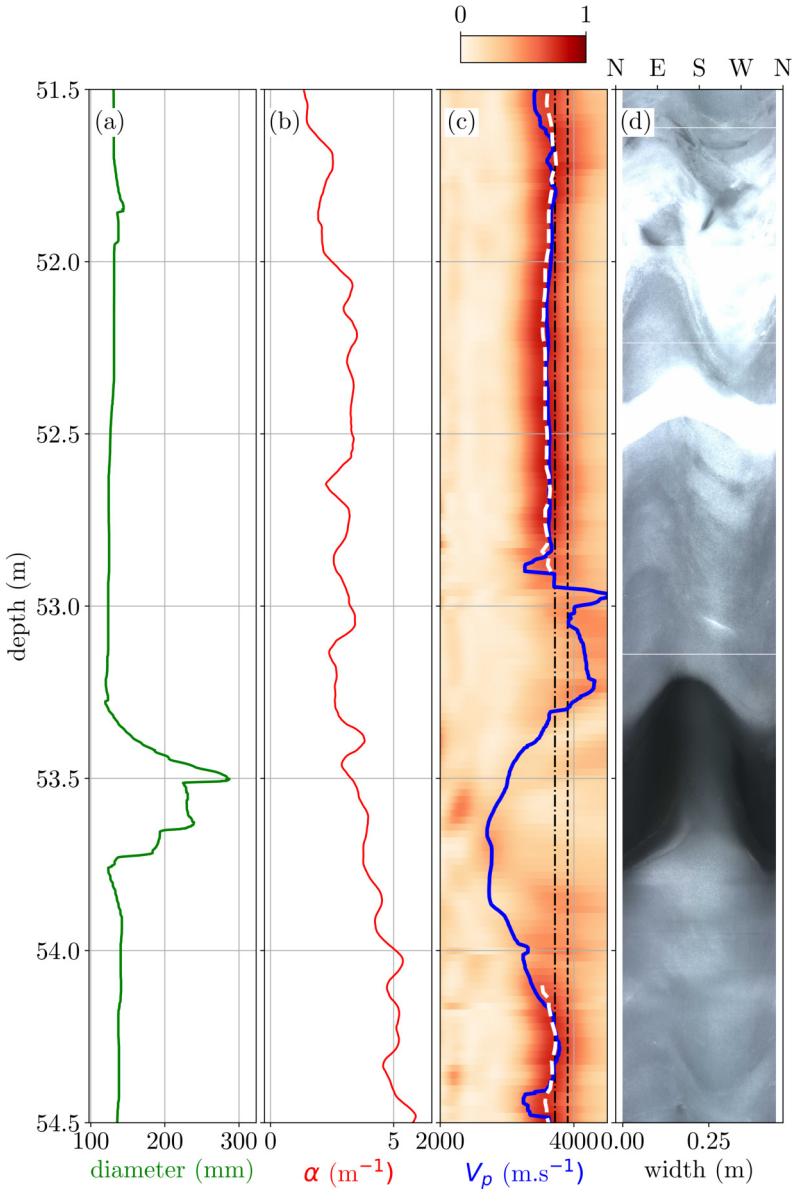

Figure 5. Logs from the borehole probe from 51.5 to 54.5 m depth. *(a)* Diameter measured by the mechanical caliper. *(b)* Acoustic absorption and *(c)* V_p picking using semblance analysis (white dashed line) or time-of-arrival regression (blue line). *(d)* Oriented optical log horizontally scaled by the average mean diameter given by the caliper.

https://doi.org/10.5194/egusphere-2025-5714
Preprint. Discussion started: 19 December 2025

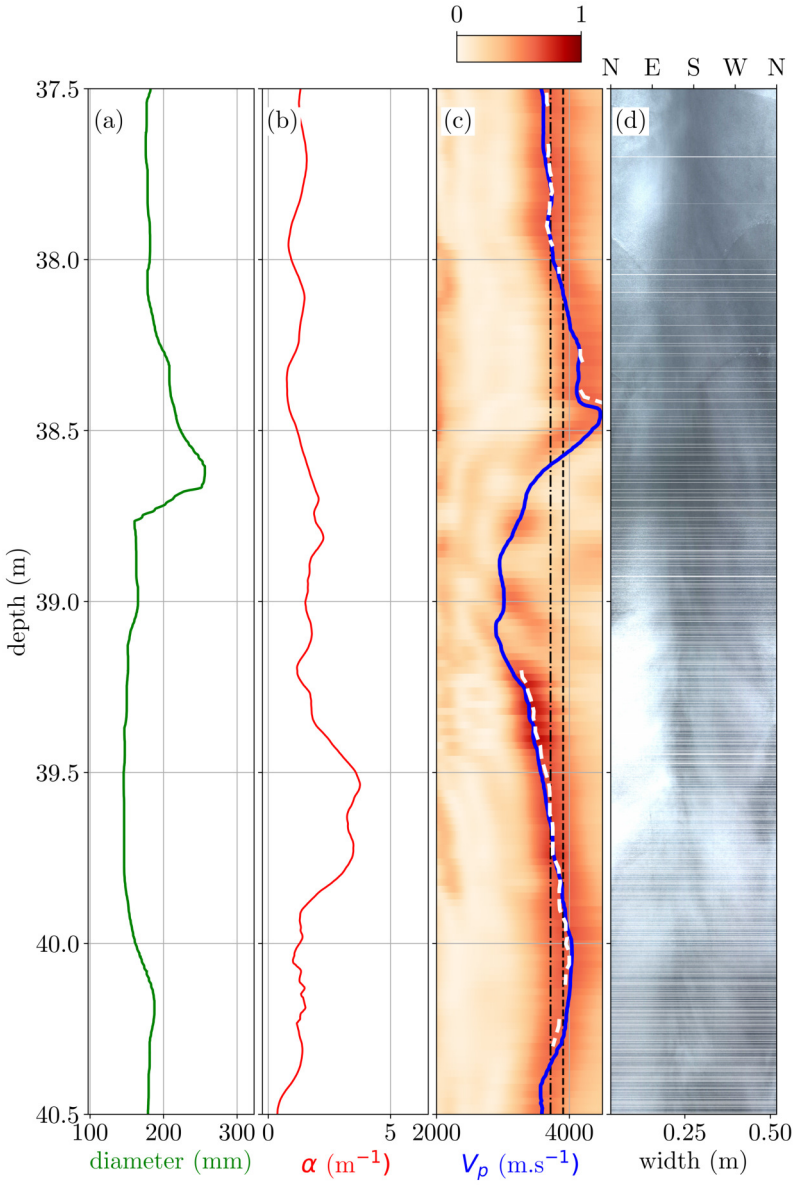

Figure 6. Logs from the borehole probe from 37.5 to 40.5 m depth. *(a)* Diameter measured by the mechanical caliper. *(b)* Acoustic absorption and *(c)* V_p picking using semblance analysis (white dashed line) or time-of-arrival regression (blue line). *(d)* Oriented optical log horizontally scaled by the average mean diameter given by the caliper.

https://doi.org/10.5194/egusphere-2025-5714
Preprint. Discussion started: 19 December 2025

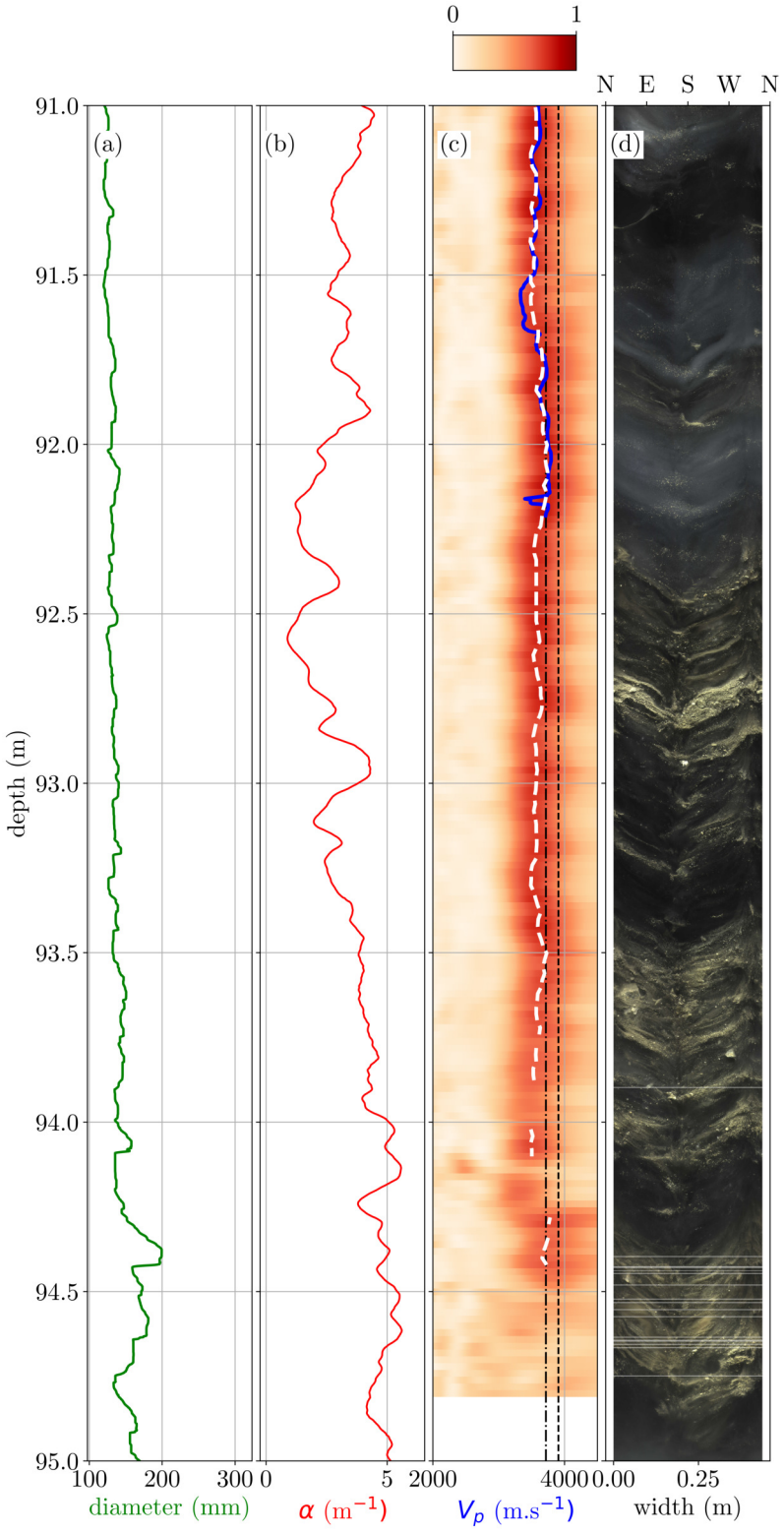

Figure 7. Logs from the borehole probe from 91 to 95 m depth. *(a)* Diameter measured by the mechanical caliper. *(b)* Acoustic absorption and *(c)* V_p picking using semblance analysis (white dashed line) or time-of-arrival regression (blue line). *(d)* Oriented optical log horizontally scaled by the average mean diameter given by the caliper.

https://doi.org/10.5194/egusphere-2025-5714
Preprint. Discussion started: 19 December 2025

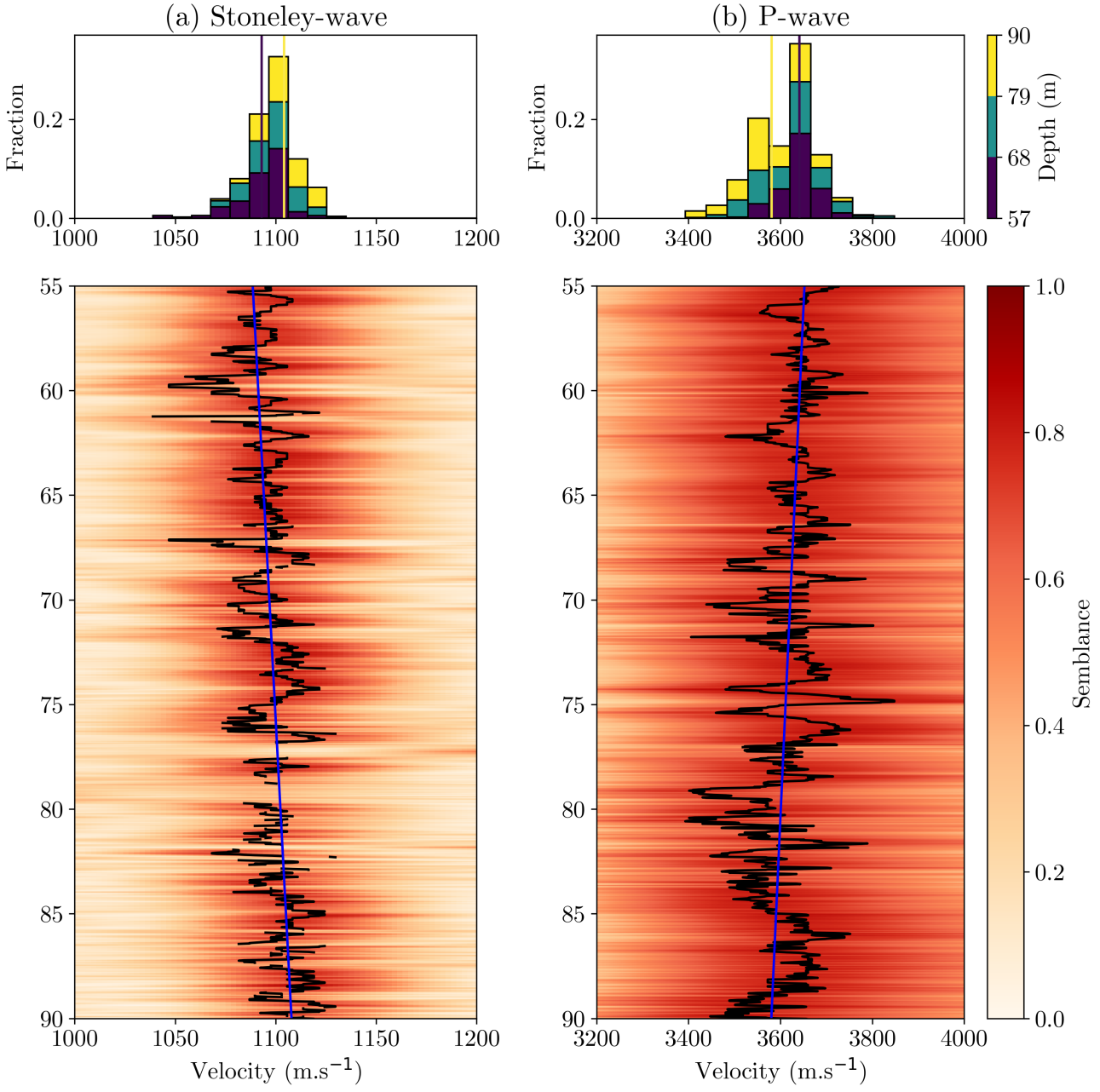

Figure 8. *(a)* Stoneley-wave and *(b)* P-wave velocities (black curve) as a function of depth, measured using semblance analysis. The blue line shows the linear regression fit from 20 to 94 m depth. The velocity distribution with depth is represented by the color-coded bar graph with the corresponding mean value distribution between [57-68] and [79-90] m (purple and yellow vertical line).

https://doi.org/10.5194/egusphere-2025-5714
Preprint. Discussion started: 19 December 2025

3.2 Ice deformation

3.3 Glacier flow acceleration link to drainage events

Two hydrological drainage events were observed between 15 September 2024 and 15 December 2024.

The first event occurred between 25 and 30 September 2024. Intense liquid precipitation was recorded between 26 September at 12:00 and 27 September, with a total accumulation of 89 mm at the Boccalatte weather station (3300 m a.s.l.) (Fig. 9(c)). This rainfall event coincided with an acceleration of glacier surface velocity, measured at the GNSS station located near the borehole, from an initial value of approximately 65 m yr^{-1} to 90 m yr^{-1}, reached at midnight on 27 September 2024 (Fig. 9(a)). Subsequently, on 30 September 2024, the piezometer installed in the borehole recorded a water pressure drop at the glacier base equivalent to 15% of the ice overburden pressure. The seismic energy recorded between 10 and 50 Hz is used as a proxy for torrent discharge (Fig. 9(d,e)). During the rainfall, both torrents exhibited a peak in seismic energy, which was also detected by the seismometer on the glacier (Fig. 9(f)). A second peak was observed on 1^{st} October 2024, following the pressure drop, in both the right- and left-bank torrents, and is likely related to enhanced discharge caused by basal drainage (Fig. 9(d,e)). These observations indicate a drainage event on 30 September 2024, likely triggered by the intense rainfall that occurred between 26 and 27 September. This period is highlighted in gray in Fig. 9.

A second event was recorded around 20 November 2024. In this case, a stronger velocity increase was observed, reaching up to 140 m yr^{-1}, but without a corresponding pressure drop in the borehole. This velocity increase coincided with enhanced seismic activity on the glacier (Fig. 9(f)) and a peak in seismic energy near the left-bank torrent (Fig. 9(e)), but not in the right-bank torrent (Fig. 9(d)). This event does not appear to have been triggered by rainfall, as only moderate solid precipitation occurred during this period, consistent with the negative air temperatures (Fig. 9(c)).

Both events are characterized by marked increases in glacier velocity associated with enhanced seismic energy on the glacier and in the torrents. The increase in torrent seismic energy is interpreted as a signature of greater discharge caused by basal water drainage. Notably, during the second event, only the left-bank torrent appears to have been affected, whereas during the first event both torrents showed increased discharge. These observations highlight the complexity and variability of basal hydrology system.

3.3.1 Mean strain rate

The initial date from which each inclinometer is assumed to be coupled with the ice was identified from the raw angle time series and set to 17 September 2024 for inclinometers below 65 m depth (Fig. D1). For the shallower instruments the initial date may differ, as closing the borehole is more difficult where stresses are weaker. From these tilt time series, strain rates were computed using Eq. 5, assuming that the angle evolution is explained by shear deformation along the flow direction. The distribution of strain rates between 17 September 2024 and 6 February 2025 is summarized by the median, with the interquartile range (25th–75th percentiles) (Fig. 10(a)).

To estimate local basal sliding, two methods were applied. The first is based on discrete integration of the tiltmeter data, while the second fits the strain rate profile using the fSIA approximation (Eq. 8) in order to reduce sensitivity to local strain

https://doi.org/10.5194/egusphere-2025-5714
Preprint. Discussion started: 19 December 2025

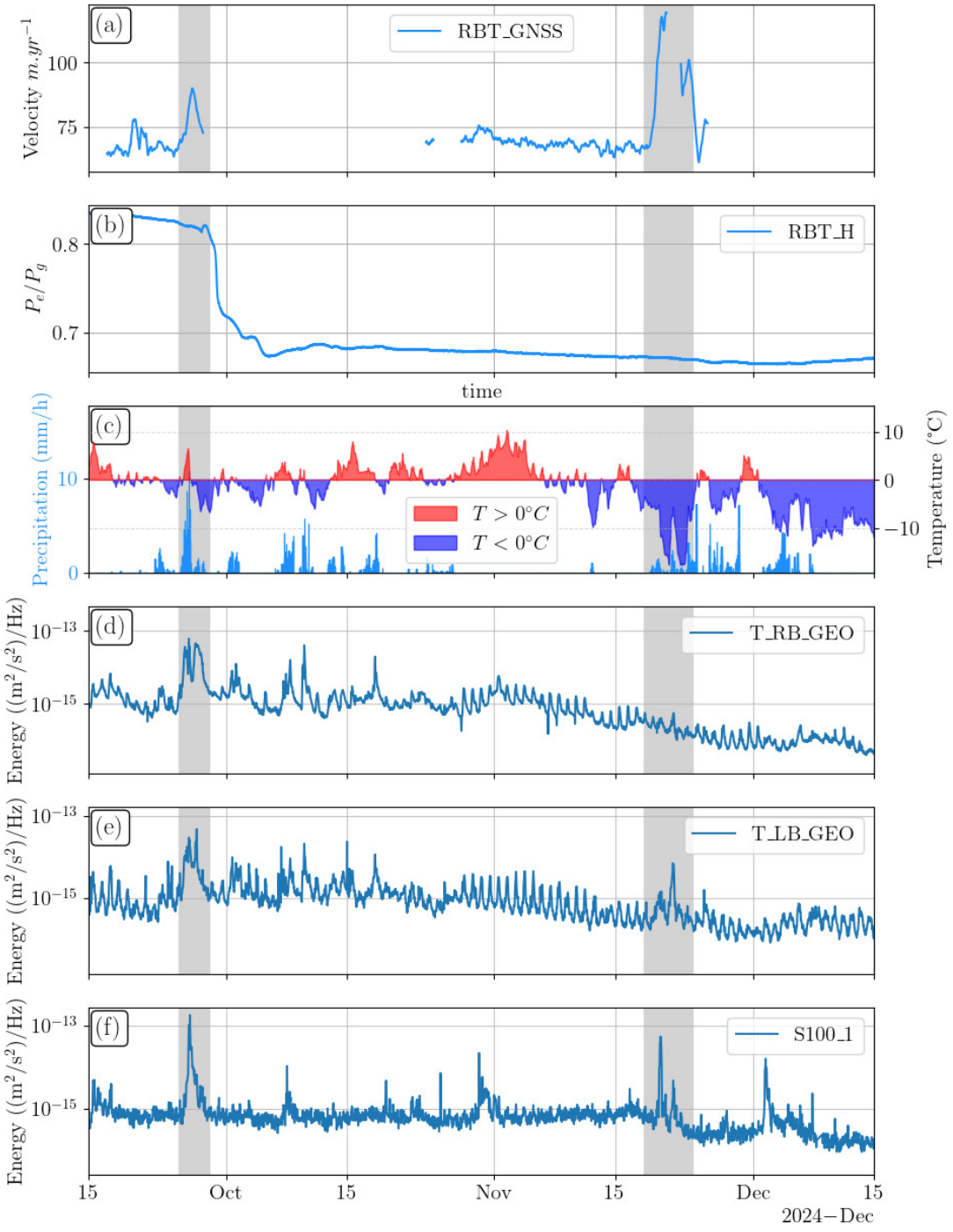

Figure 9. Time series recorded on the Planpincieux Glacier between 15 September and 15 December 2024. *(a)* Surface velocity of the glacier measured by the GNSS station located near the borehole. *(b)* Normalized pressure recorded at the ice–bedrock interface in the borehole. *(c)* Precipitation and air temperature recorded by the automatic weather station near the Planpincieux Glacier at 3300 m a.s.l. Seismic energy integrated between 10 and 50 Hz for the seismometers located near the right-bank torrent *(d)*, the left-bank torrent *(e)*, and on the glacier *(f)*.

https://doi.org/10.5194/egusphere-2025-5714
Preprint. Discussion started: 19 December 2025

	A ($Pa^{-n}.yr^{-1}$)	**n**	**f**	α (°)
fit A and n	7.52×10^{-41}	7.76	**0.5**	**19.5379**
fit A	2.35×10^{-16}	**3**	**0.5**	**19.5379**

Table 1. Parameters corresponding to the different fits of Eq. 8. The bold parameters are fixed values.

heterogeneities. The surface slope is estimated from the surface DEM as 19.5° and the shape factor as 0.5 using Nye (1965) tabulation (Appendix E). Two different fits of the inclinometer data were performed: the first involved fitting both A and n, while the second fixed the stress exponent to $n = 3$. Fitting with two free parameters provides greater flexibility than the single-parameter fit and therefore yields better agreement with the observations (Fig. 10(a)). Table 1 shows the different values obtained from the curve fitting.

The velocity profiles were reconstructed by combining the inferred deformation rates with the mean surface velocity measured by the GNSS (71 m yr^{-1}) over the same period. Figure 10(b) shows the velocity profiles derived from both fitting approaches and from the discrete integration. The results obtained from the discrete integration and from the fit with $n = 7.8$ yield similar basal sliding velocities of 46.1 m yr^{-1} (discrete method) and 48.5 m yr^{-1} (fitted method), whereas the fit with a fixed $n = 3$ tends to overestimate the contribution of deformation and consequently underestimate the basal velocity. Overall, the proportion of deformation contributing to the total surface velocity is estimated at 35% (discrete method) and 32% (fitted method, $n = 7.8$).

Figure 10(c) shows the estimated horizontal stress τ_{xz} obtained using the SIA, fSIA ($f = 0.5$), and the three-dimensional Elmer/Ice model, as well as the effective stress τ_e from the Elmer/Ice simulation. The corresponding fluidity values derived from the strain rate curve fitting are shown alongside the depth-dependent fluidity computed using the three-dimensional stress field. A reference value of 75 MPa^{-3} yr^{-1} from Cuffey and Paterson (2010) is also included for comparison. The relationship between fluidity A and water content W is derived from Duval (1977), following the approach of Roldán-Blasco et al. (2024), by assuming a reference value of $A = 50$ MPa^{-3} yr^{-1} for $W = 0$:

$$W = \frac{1}{2.34}\left(\frac{A}{50} - 1\right). \tag{9}$$

Considering a variable fluidity $A(z)$, values up to 600 MPa^{-3} yr^{-1} are obtained, corresponding to a theoretical enhancement in fluidity equivalent to a water content of approximately 8%.

These estimations are sensitive to the stress field computed with Elmer/Ice, which depends primarily on the accuracy of the bedrock topography. Another source of uncertainty arises from the assumption that the strain rate derived from tilt evolution is solely due to horizontal shearing, whereas compressive deformation may also influence the angle evolution (Keller and Blatter, 2012). Consequently, in the deepest layers, the shear strain rate may be overestimated, leading to an overestimation of the fluidity.

https://doi.org/10.5194/egusphere-2025-5714
Preprint. Discussion started: 19 December 2025

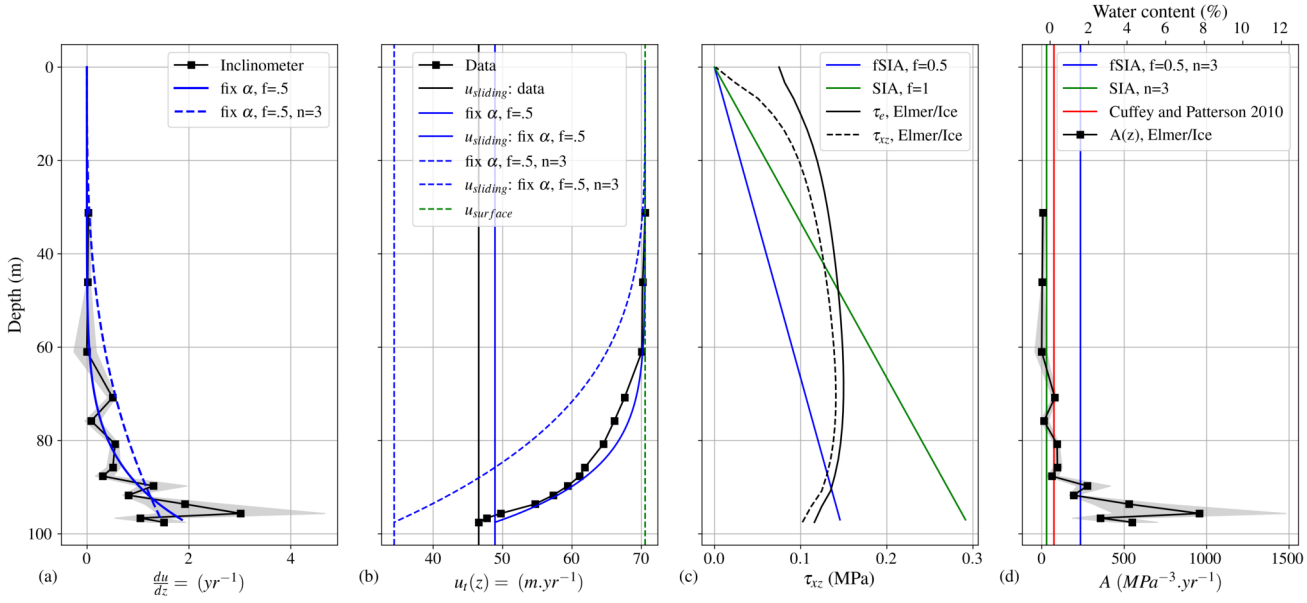

Figure 10. *(a)* Average strain rate profile measured by the inclinometers (black squares), with the interquartile range (25th–75th percentiles) shown in gray. The blue line represents the best-fit fSIA model defined in Table 1. *(b)* Reconstructed velocity profile combining the surface velocity measured by GNSS (green dashed line) with the discrete inclinometer data (black squares) and the fitted curve (blue line). The vertical black and blue lines indicate the basal velocities obtained from both methods. *(c)* Estimation of τ_{xz} using the SIA, fSIA ($f = 0.5$), and the three-dimensional Elmer/Ice model. *(d)* Estimation of fluidity assuming a constant A with depth for both SIA and fSIA stresses, together with the depth-dependent fluidity variations derived from Elmer/Ice stress estimations. A value given by Cuffey and Paterson (2010) is also shown as reference.

3.3.2 Localized deformation

Figure 11 shows the evolution of the strain rate $\frac{du}{dz}$ from 1^{st} September 2024 to 1^{st} February 2025 for the inclinometers located between 85 and 98 m depth, together with the optical image of the borehole wall over this section. The two identified basal drainage events are highlighted in gray.

Before the first drainage period, the strain rate remained relatively constant across the inclinometer chain. The deeper layers exhibited higher values, reaching 0.39, 0.84, and 0.93 m yr^{-1} at 91.8, 93.6, and 95.6 m depth, respectively (25 October 2024). During the drainage event, the strain rate increased substantially, reaching 0.84, 1.66, and 1.54 m yr^{-1} at the corresponding depths (30 October 2024). In these layers, the strain rate approximately doubled, whereas the surface velocity increased by less than a factor of 1.5, rising from 65 m yr^{-1} to 90 m yr^{-1}. This increase in strain rate was observed across all inclinometers except the one at 87.6 m depth.

About ten days after the end of the drainage event (9–31 October 2024), a pronounced increase in strain rate was recorded at 93.6 m depth, where a high concentration of debris was identified in the optical imagery. The strain rate reached up to

https://doi.org/10.5194/egusphere-2025-5714
Preprint. Discussion started: 19 December 2025

20 yr^{-1}, more than 20 times the pre-drainage values. At the same time, no significant changes were detected in the overlying layer (Fig. 11), which is characterized by lower debris content, higher P-wave velocity, and lower absorption α. Below the debris-rich layer, a more complex behavior was observed: the strain rate exhibited a rapid inversion from negative to positive shear of comparable magnitude ($\pm$40 yr^{-1}), but delayed by about one week, starting on 15 October 2024 (Fig. 11). This layer does not appear to contain a high concentration of debris, although no sonic logging data are available at this depth, and the optical logger images may still have been affected by suspended particles present in the borehole water (Fig. 11). The deepest inclinometer, below 96 m depth, did not record any significant variation in strain rate during this period.

During the second drainage event in December, the inclinometers at 93.6 and 95.6 m depth continued to exhibit high strain rates. In addition, the inclinometer at 89.7 m depth recorded a peak of up to 15 yr^{-1}, whereas the other inclinometers did not show a clear response to this event where no clear structural heterogeneity is visible on the optical image.

These observations of strain rate evolution in the layers close to the bedrock interface reveal strong spatial and temporal variability, which appears correlated with structural heterogeneities and their response to basal drainage events.

4 Discussion

4.1 Structural heterogeneities characterization

Optical and sonic logging provide valuable insights into the structural heterogeneities of the glacier. Several features are identifiable, including foliation planes likely associated with impurity content (Fig. 5 between 51.5 and 52.5 m), open water-filled crevasses (Figs. B2 and 5 between 52.5 and 54.5 m), closed crevasses (Figs. 6 and B4), and granitic debris-rich layers near the bedrock interface (Fig. 7).

The dust planes extracted from the optical log (Fig. 3*(a)*) are likely related to the seasonal stratification produced by snow accumulation. Their orientation therefore results from the slope at the accumulation site, combined with the solid-body rotation imposed by advection along the flow line. Nevertheless, the plane orientations progressively rotate with depth toward alignment closer to the local surface slope at the logging site (blue square, Fig. 3*(a)*). This suggests that these planes are influenced by the foliation developed during ice deformation. As deformation is stronger in the deeper layers (Fig. 10), the original accumulation-plane orientation is increasingly overprinted by the deformation-induced foliation. This interpretation is supported by the orientation of the granite-debris layers (Fig. 3*(d)*), which cluster near the slope-parallel plane but also align with the flow direction (blue triangle, Fig. 3).

In contrast, the orientation of open and closed crevasses appears to reflect the local stress field. The open crevasses do not show any preferred orientation, whereas the closed crevasses exhibit clustering aligned with the flow direction (blue triangle, Fig. 3*(c)*). This observation suggests that the stress conditions along the flow direction are predominantly compressive in the borehole area. Such compression is consistent with the borehole's location upstream of a bedrock depression (Fig. 1(b)). In this configuration, ice on the plateau (Fig. 1(c), 0–200 m from the borehole) flows more slowly than the ice upstream (Fig. 1(c), distance < 0), generating compressive stresses that tend to close crevasses aligned with the flow direction. The apparent "closed"

https://doi.org/10.5194/egusphere-2025-5714
Preprint. Discussion started: 19 December 2025

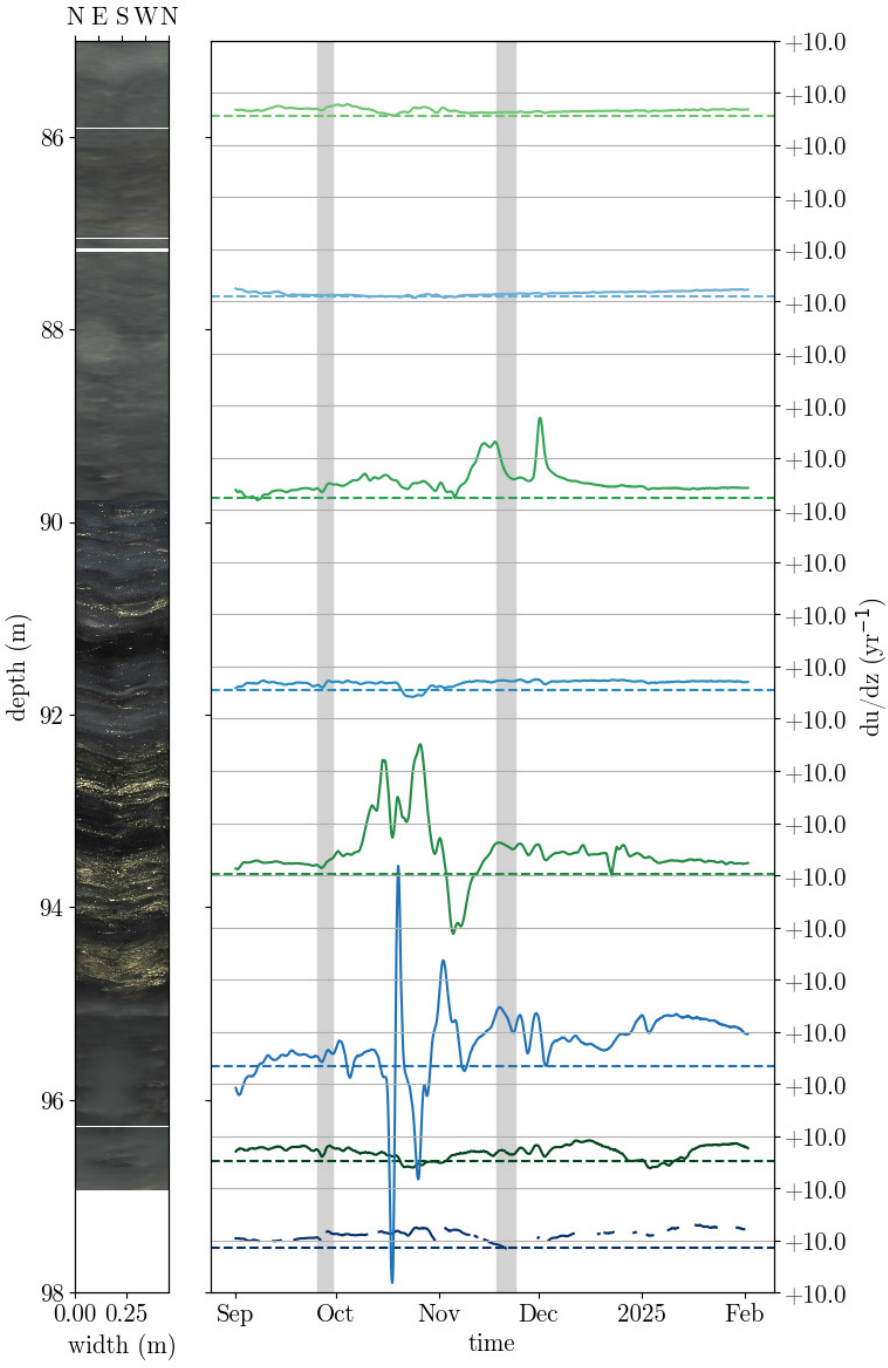

Figure 11. Strain rate evolution between 1^{st} September 2024 and 1^{st} February 2025, measured by the inclinometer chain at depths between 85 and 97 m, together with the corresponding optical stratigraphy. The dashed lines indicate the positions of the inclinometers, while the solid curves show the strain rate $\frac{du}{dz}$, scaled according to the left axis. Each color corresponds to data from one inclinometer. The optical stratigraphy is constructed from two optical logs: the first acquired immediately after drilling, and the clearer one acquired one day later between 90 and 95 m depth. Consequently, the image obtained immediately after drilling may appear blurrier than the one recorded between 90 and 95 m depth (Fig. B1).

https://doi.org/10.5194/egusphere-2025-5714
Preprint. Discussion started: 19 December 2025

crevasse observed in the optical log but showing the P-wave signature of a water-filled fracture (Fig. 6) further supports this interpretation, indicating that crevasse closure is still active around the borehole.

The average P-wave velocity measured by the acoustic logger is about 3600 m s^{-1}. This value is consistent with results from other temperate glaciers using dense seismic node arrays, such as at Argentière Glacier (Gimbert et al., 2021). It is, however, lower than theoretical predictions for a polycrystal with a uniform texture (3726 m s^{-1}). Laboratory measurements on natural ice samples with strong single-maximum fabrics (Lutz et al., 2022) report velocities ranging from 3600 m s^{-1} (orthogonal to the single maximum) to 3900 m s^{-1} (parallel to the single maximum).

At Planpincieux, the P-wave velocity was measured vertically in a borehole drilled in the central part of the glacier (Fig. 1), away from shear margins. Deformation in this region is likely dominated by horizontal shearing aligned with the flow direction. Both experimental and numerical studies have shown that horizontal shear promotes the development of a vertical single-maximum texture, with or without the influence of dynamic recrystallization (Bouchez and Duval, 1982; **?**; Gillet-Chaulet et al., 2006; Chauve et al., 2024). If such a texture were present, it would tend to increase the P-wave velocity above the uniform-texture value. Instead, we observe a lower velocity. Moreover, the P-wave velocity is decreasing with depth at -2 m s^{-1}.m^{-1}. If interpreted as a texture effect, this would imply a weakening fabric at depth, which contradicts expectations that texture development should strengthen with increasing strain in deeper ice (Fig. 10). Texture alone therefore cannot explain the observed velocities.

Other factors must be considered. Water content, either stored in crevasse networks or as interstitial water, is expected to reduce acoustic velocities. Rock debris is another possible influence: debris-rich ice is common below 90 m depth (Fig. 7). Since P-wave velocities in granite are 5000–6000 m s^{-1} (Leet, 1933), inclusions could affect the average velocity depending on their size relative to the acoustic wavelength. At 15 kHz, the emitted sonic wavelength is 24 cm for a velocity of 3600 m s^{-1}. As the observed particles are much smaller (Fig. 7), effective velocities should approximate a weighted average of the ice and debris phases (Mavko et al., 2011). However, no significant differences are observed between debris-rich ice (Fig. 7) and debris-free ice (Fig. 5 between 51.5 and 52.5 m), suggesting that debris content has little influence on the measured P-wave velocity or other heterogeneity counter this effect.

Water content, by contrast, provides a more consistent explanation. Since P-waves propagate more slowly in water (1500 m s^{-1}), the presence of liquid inclusions reduces the velocity. This effect is directly observed when the logger crosses a crevasse (Fig. 5). If the velocity reduction from 3726 to 3600 m s^{-1} is attributed entirely to water, the implied fraction is 5.6% ($3600 = 3726 \times (1 - 0.056) + 1500 \times 0.056$). This estimate is higher than previous determinations of water content in temperate glaciers obtained by calorimetric measurements (Vallon et al., 1976; Lüthi et al., 2025).

A depth-dependent trend is also visible in both P-wave and Stoneley-wave velocities (Fig. 8). The P-wave velocity decreases at a rate of -2 m s^{-1}.m^{-1}, which can be interpreted as a water-content increase of 3.8×10^{-4} m^{-1}, corresponding to approximately 2% over 50 m of depth. An independent estimation of water content can be obtained by assuming that the observed variation in fluidity with depth is primarily controlled by changes in water content, as proposed by Roldán-Blasco et al. (2024). The fluidity values $A(z)$ estimated for the Planpincieux Glacier (Fig. 10(d)) are comparable to those reported for the Argentière

https://doi.org/10.5194/egusphere-2025-5714
Preprint. Discussion started: 19 December 2025

Glacier (Roldán-Blasco et al., 2024). Those authors showed that a 2% variation in water content can account for the observed range in fluidity. A similar conclusion can therefore be drawn here.

Both the variation in fluidity and the trend in P-wave velocity can be explained by the same increase in water content with depth, supporting this hypothesis.

If the decrease in P-wave velocity is due to increasing water content, the mechanism should involve a reduction in the bulk modulus (Eq. 1). White's model (Eq. 2) predicts that this would also reduce the Stoneley-wave velocity. However, the Stoneley-wave measurements instead show an increase with depth at +0.55 m $s^{-1}.m^{-1}$. In petrophysical studies, Stoneley-wave velocities are strongly correlated with permeability: higher permeability leads to lower velocities (Saxena et al., 2018). Assuming this relationship holds for ice, the Planpincieux results suggest that permeability decreases with depth, even as water content increases. A plausible explanation is that the nature of water storage changes with depth. In the middle part of the glacier, water is mainly stored in open crevasses (Figs. 3(b,c), 5), forming a permeable network that slows Stoneley-waves. At greater depths, fracture opening is suppressed by higher confining pressure, reducing permeability and raising Stoneley-wave velocities. The higher water content at depth is therefore likely to be interstitial, stored within the ice matrix. Interstitial water is expected to accumulate in regions of high deformation due to shear heating (Vallon et al., 1976) and strain concentration at grain boundaries caused by ice plastic anisotropy (De La Chapelle et al., 1998; Grennerat et al., 2012; Chauve et al., 2015). Additional strain concentration around rock inclusions may further enhance interstitial water storage. This effect is more likely to enhance water content in the deepest part of the glacier where high debris concentrations is observed, likely introduced by basal erosion.

These processes may explain the contrasting depth trends of P-wave and Stoneley-wave velocities. Nevertheless, further theoretical and laboratory studies are needed to fully understand acoustic wave propagation in multiphase glacier ice. Such work could help establish a framework for inverting borehole acoustic log data to quantify water content, debris concentration, and permeability.

4.2 The link between structural heterogeneity and strain localization

The mean strain rate measured by the inclinometer chain reaches values up to 2 yr^{-1} down to 90 m depth, corresponding to approximately one third of the surface velocity being accommodated by internal deformation of the ice (Fig. 10). Closer to the bedrock interface, below 90 m depth, strong variations in strain rate are recorded within localized layers (Fig. 11). These variations show a clear temporal correlation with basal drainage events, evidenced by increases in seismic energy recorded by the seismometers, which reflect enhanced discharge in the torrents draining the glacier, and by the concurrent surface velocity acceleration recorded by the GNSS (Fig. 9).

The first event occurred following heavy rainfall of 89 mm over a period of one and a half days, which likely acted as the trigger for the 40% increase in glacier velocity (Fig. 9). The intense rainfall likely reduced basal friction, leading to the observed acceleration, consistent with previous observations of hydrologically induced speed-ups (Togaibekov et al., 2024). During this phase, the strain rate recorded by all sensors increased by a similar proportion (Fig. 11).

https://doi.org/10.5194/egusphere-2025-5714
Preprint. Discussion started: 19 December 2025

At the end of September and beginning of October, as the surface velocity decreased, the piezometer recorded a pressure drop, while the torrent seismometers detected increased discharge. This phase is interpreted as the basal drainage itself, likely resulting from the opening of subglacial channels during the high-velocity phase and the additional water input from rainfall. Approximately one week after the drainage event, strong strain localization, reaching up to 25 yr^{-1}, developed in the layer at 93.6 m depth, where the optical log shows a high concentration of granite debris (Fig. 11). Meanwhile, the other inclinometers recorded steady strain rates. A few days later, the inclinometer below (95.6 m depth) exhibited a more complex response, characterized by rapid alternations between negative and positive shear. The acceleration of strain rate within the debris-rich layer indicates a stress perturbation near the bedrock interface.

These observations raise two main questions: (i) why is there a delay between the basal drainage and the observed strain rate increase? and (ii) why does the strain rate increase remain localized in specific ice layers?

Considering the ice deformation processes, we interpret the sequence of events as follows:

- After the rainfall-triggered velocity increase and prior to the drainage, the strain rate in the borehole rises in response to the overall glacier acceleration. Although the global sliding friction decreases, the glacier does not behave as a rigid block; instead, spatially variable frictional resistance creates zones where stress is locally concentrated, resulting in enhanced strain (gray areas, Figs. 9 and 11).

- Once drainage of the basal hydrological system occurs, the glacier slows down (Fig. 9) as water stored in subglacial cavities is released. This drainage modifies the basal friction, leading to a redistribution of stresses within the ice column.

- In response to this stress reorganization, strong strain localization develops in the debris-rich layer at 93 m depth (Fig. 11). The debris were likely incorporated into the ice matrix through basal erosion at a topographic bump. The mechanical behavior of debris-laden ice remains poorly constrained (Moore, 2014, for review), and may be further complicated by the presence of liquid water in temperate ice (Duval, 1977; Schohn et al., 2025). In this configuration, the debris-rich layer appears to exhibit enhanced fluidity, potentially amplified by the production of interstitial water through stress localization at particle interfaces. This rate-weakening effect could sustain the high strain rates observed in this layer for over a month.

The second event, observed in December, shows the same sequence of processes. The main differences are that (i) this event was not triggered by rainfall, and (ii) the layer exhibiting the strongest strain rate increase, located at 89.6 m depth, displays less pronounced structural heterogeneity. Such changes may also reflect the ongoing glacier flow, as local bedrock rugosities or basal-ice heterogeneities are likely to evolve over time.

Both drainage events highlight the importance of mechanical heterogeneity in controlling the strain rate variability observed near the bedrock interface. They also suggest potential mechanisms that could influence the formulation of friction laws derived from numerical models at the cavity scale (Gagliardini et al., 2007). In these models, the relationship between basal shear stress τ_b and basal velocity u_b is obtained by simulating ice flow with homogeneous mechanical properties and integrating the horizontal component of the basal velocity (Fig. 12(a)). However, the observations from the Planpincieux Glacier raise

https://doi.org/10.5194/egusphere-2025-5714
Preprint. Discussion started: 19 December 2025

questions about the role of heterogeneities, which may locally weaken the ice in layers located above bedrock rugosities, thereby partially masking their mechanical effect (Fig. 12(a)).

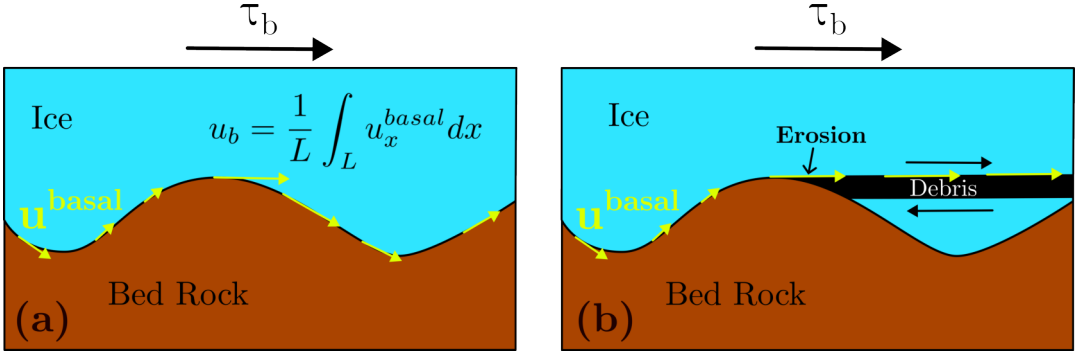

Figure 12. Schematic representation of the computation of the friction law *(a)* and of the potential effect of debris-layer heterogeneity *(b)*.

5 Conclusions

This study presents an investigation of the relationship between structural heterogeneities and deformation in glacier ice at Planpincieux Glacier (Mont Blanc massif). A borehole was drilled on the lower plateau, where a set of complementary instruments—including an optical televiewer, a full-waveform sonic logger, a piezometer, and an inclinometer-chain were deployed. These measurements, supported by GNSS and seismic monitoring, allowed the characterization of englacial structures and strain rate evolution during hydrological draining events.

Two main families of structural heterogeneities were identified from optical and sonic logging: (i) open and closed crevasses in the upper 60 m, and (ii) debris-rich layers near the bedrock interface. The analysis of acoustic waveforms revealed continuous trends of both P- and Stoneley-wave velocities with depth. P-wave velocity decreases from 3640 to 3580 m s^{-1}, suggesting a progressive increase in interstitial water content, whereas the Stoneley-wave velocity shows an opposite trend, indicating reduced permeability. These contrasting evolutions highlight the coexistence of water-filled fractures and interstitial water within glacier ice, demonstrating a high degree of complexity for the structural heterogeneity. Nevertheless, a complete inversion of the structural heterogeneities remains a complex task that will require better constraints from laboratory experiments to quantify the influence of each physical parameter on wave-propagation behavior.

The inclinometer data show that roughly one-third of the surface velocity is accommodated by internal deformation, with strong strain localization in layers close to the bedrock. Strain rate peaks coincide with hydrological drainage events and are particularly pronounced in debris-rich ice, suggesting a coupling between mechanical heterogeneity, transient basal hydrology, strain weakening, and strain localization. These observations challenge the common assumption of homogeneous ice rheology in basal friction models and emphasize the need to incorporate the effects of structural and mechanical heterogeneities when formulating friction laws at the cavity scale. To achieve this, future studies should aim to develop well-defined constitutive

https://doi.org/10.5194/egusphere-2025-5714
Preprint. Discussion started: 19 December 2025

laws capable of accounting for the complexity of such heterogeneities, including the role of interstitial water (Duval, 1977; Schohn et al., 2025) and debris inclusions (Moore, 2014).

Code and data availability. Python code related to the production of the results is available on a GitLab repository https://gricad-gitlab.univ-grenoble-alpes.fr/mecaiceige/publication/chauve_et_al_2025_planpincieux_logger. The data are available on demand.

Author contributions. **TC** Investigation, Conceptualization, Methodology, Writing - Original Draft, Formal analysis, Software. **FG** Conceptualization, Methodology, Formal analysis, Resources. **AG** Conceptualization, Methodology, Formal analysis, Software. **OG** Conceptualization, Methodology, Writing - Review Editing, Supervision. **LP** Investigation. **AR** Investigation. **OL** Investigation. **FT** Funding acquisition, Project administration. **WB** Investigation. **PDS** Investigation. **LM** Investigation. **PP** Investigation.

Competing interests. The authors declare that they have no competing interests.

Acknowledgements. The authors are grateful to the *Fondo per lo sviluppo e la coesione (FSC) in anticipazione sul ciclo di programmazione 2021-2027* for funding this study *Ghiacciai valdostani sentinelle del cambiamento climatico: iniziative di ricerca e innovazione - CUP E79J21002860003*. We also thank the Courmayeur Alpine Guides for their assistance during the fieldwork and for ensuring safety on the glacier during the instrument deployment and all the people that were ponctually involves in the field work (Emmanuel Lemeur, Tifenn Le Bris, Hugo Rousseau, Alexandre Michel, Olivier Coutant, Hugo Jacquet). We acknowledge the use of ChatGPT (https://chat.openai.com/) to assist with English grammar and language editing.

https://doi.org/10.5194/egusphere-2025-5714
Preprint. Discussion started: 19 December 2025

References

Adams, C. J. C., Iverson, N. R., Helanow, C., Zoet, L. K., and Bate, C. E.: Softening of Temperate Ice by Interstitial Water, Frontiers in Earth Science, 9, https://doi.org/10.3389/feart.2021.702761, 2021.

Akhmetsafin, R., Dubinskii, V., and Patterson, D.: Hilbert-semblance method for acoustic logging data processing, Russian Geology and Geophysics, 49, 692–697, https://doi.org/10.1016/j.rgg.2007.12.012, 2008.

Aki, K. and Richards, P. G.: Quantitative seismology, University Science Books, Sausalito, Calif., 2. ed. edn., ISBN 0935702962, includes bibliographical references and index, 2002.

Amundson, J. M., Truffer, M., and Lüthi, M. P.: Time-dependent basal stress conditions beneath Black Rapids Glacier, Alaska, USA, inferred from measurements of ice deformation and surface motion, Journal of Glaciology, 52, 347–357, https://doi.org/10.3189/172756506781828593, 2006.

Azuma, N., Wang, Y., Mori, K., Narita, H., Hondoh, T., Shoji, H., and Watanabe, O.: Textures and fabrics in the Dome F (Antarctica) ice core, Annals of Glaciology, 29, 163–168, https://doi.org/10.3189/172756499781821148, 1999.

Booth, A. D., Christoffersen, P., Schoonman, C., Clarke, A., Hubbard, B., Law, R., Doyle, S. H., Chudley, T. R., and Chalari, A.: Distributed Acoustic Sensing of Seismic Properties in a Borehole Drilled on a Fast-Flowing Greenlandic Outlet Glacier, Geophysical Research Letters, 47, https://doi.org/10.1029/2020gl088148, 2020.

Bouchez, J. L. and Duval, P.: The Fabric of Polycrystalline Ice Deformed in Simple Shear: Experiments in Torsion, Natural Deformation and Geometrical Interpretation, Texture, Stress, and Microstructure, 5, 171–190, https://doi.org/10.1155/tsm.5.171, 1982.

Chauve, T., Montagnat, M., and Vacher, P.: Strain field evolution during dynamic recrystallization nucleation; A case study on ice, Acta Materialia, 101, 116–124, https://doi.org/10.1016/j.actamat.2015.08.033, 2015.

Chauve, T., Montagnat, M., Dansereau, V., Saramito, P., Fourteau, K., and Tommasi, A.: A physically-based formulation for texture evolution during dynamic recrystallization. A case study of ice, Comptes Rendus. Mécanique, 352, 99–134, https://doi.org/10.5802/crmeca.243, 2024.

Cuffey, K. M. and Paterson, W. S. B.: The Physics of Glaciers, Elsevier Science Technology, San Diego, 4th ed. edn., ISBN 9780080919126, description based on publisher supplied metadata and other sources., 2010.

De La Chapelle, S., Castelnau, O., Lipenkov, V., and Duval, P.: Dynamic recrystallization and texture development in ice as revealed by the study of deep ice cores in Antarctica and Greenland, Journal of Geophysical Research: Solid Earth, 103, 5091–5105, 1998.

De La Chapelle, S., Milsch, H., Castelnau, O., and Duval, P.: Compressive creep of ice containing a liquid intergranular phase: Rate-controlling processes in the dislocation creep regime, Geophysical Research Letters, 26, 251–254, https://doi.org/10.1029/1998gl900289, 1999.

Dematteis, N., Luzi, G., Giordan, D., Zucca, F., and Allasia, P.: Monitoring Alpine glacier surface deformations with GB-SAR, Remote Sensing Letters, 8, 947–956, https://doi.org/10.1080/2150704X.2017.1335905, 2017.

Dematteis, N., Giordan, D., Troilo, F., Wrzesniak, A., and Godone, D.: Ten-Year Monitoring of the Grandes Jorasses Glaciers Kinematics. Limits, Potentialities, and Possible Applications of Different Monitoring Systems, Remote Sensing, 13, 3005, https://doi.org/10.3390/rs13153005, 2021.

Dematteis, N., Troilo, F., Scotti, R., Colombarolli, D., Giordan, D., and Maggi, V.: The use of terrestrial monoscopic time-lapse cameras for surveying glacier flow velocity, Cold Regions Science and Technology, 222, 104 185, https://doi.org/10.1016/j.coldregions.2024.104185, 2024.

https://doi.org/10.5194/egusphere-2025-5714
Preprint. Discussion started: 19 December 2025

Derkacheva, A., Gillet-Chaulet, F., Mouginot, J., Jager, E., Maier, N., and Cook, S.: Seasonal evolution of basal environment conditions of Russell sector, West Greenland, inverted from satellite observation of surface flow, The Cryosphere, 15, 5675–5704, https://doi.org/10.5194/tc-15-5675-2021, 2021.

Doyle, S. H., Hubbard, B., Christoffersen, P., Young, T. J., Hofstede, C., Bougamont, M., Box, J. E., and Hubbard, A.: Physical Conditions of Fast Glacier Flow: 1. Measurements From Boreholes Drilled to the Bed of Store Glacier, West Greenland, Journal of Geophysical Research: Earth Surface, 123, 324–348, https://doi.org/10.1002/2017jf004529, 2018.

Durand, G., Weiss, J., Lipenkov, V., Barnola, J. M., Krinner, G., Parrenin, F., Delmonte, B., Ritz, C., Duval, P., Röthlisberger, R., and Bigler, M.: Effect of impurities on grain growth in cold ice sheets, Journal of Geophysical Research: Earth Surface, 111, https://doi.org/10.1029/2005jf000320, 2006.

Durand, G., Svensson, A., Persson, A., Gagliardini, O., Gillet-Chaulet, F., Sjolte, J., Montagnat, M., and Dahl-Jensen, D.: Evolution of the texture along the EPICA Dome C ice core, 低温科学, 68, 91–105, 2009.

Duval, P.: The role of the water content on the creep rate of polycrystalline ice., Proc. Grenoble Symposium, 1977.

Duval, P. and Lorius, C.: Crystal size and climatic record down to the last ice age from Antarctic ice, Earth and Planetary Science Letters, 48, 59–64, https://doi.org/10.1016/0012-821x(80)90170-3, 1980.

Duval, P., Ashby, M. F., and Anderman, I.: Rate-controlling processes in the creep of polycrystalline ice, The Journal of Physical Chemistry, 87, 4066–4074, https://doi.org/10.1021/j100244a014, 1983.

Fichtner, A., Hofstede, C., Kennett, B. L. N., Svensson, A., Westhoff, J., Walter, F., Ampuero, J.-P., Cook, E., Zigone, D., Jansen, D., and Eisen, O.: Hidden cascades of seismic ice stream deformation, Science, 387, 858–864, https://doi.org/10.1126/science.adp8094, 2025.

Gagliardini, O., Cohen, D., Råback, P., and Zwinger, T.: Finite-element modeling of subglacial cavities and related friction law, Journal of Geophysical Research: Earth Surface, 112, https://doi.org/10.1029/2006jf000576, 2007.

Gagliardini, O., Zwinger, T., Gillet-Chaulet, F., Durand, G., Favier, L., de Fleurian, B., Greve, R., Malinen, M., Martín, C., Råback, P., Ruokolainen, J., Sacchettini, M., Schäfer, M., Seddik, H., and Thies, J.: Capabilities and performance of Elmer/Ice, a new-generation ice sheet model, Geoscientific Model Development, 6, 1299–1318, https://doi.org/10.5194/gmd-6-1299-2013, 2013.

Gammon, P. H., Kiefte, H., and Clouter, M. J.: Elastic constants of ice samples by Brillouin spectroscopy, The Journal of Physical Chemistry, 87, 4025–4029, https://doi.org/10.1021/j100244a004, 1983.

Gerbi, C., Mills, S., Clavette, R., Campbell, S., Bernsen, S., Clemens-Sewall, D., Lee, I., Hawley, R., Kreutz, K., and Hruby, K.: Microstructures in a shear margin: Jarvis Glacier, Alaska, Journal of Glaciology, 67, 1163–1176, https://doi.org/10.1017/jog.2021.62, 2021.

Gillet-Chaulet, F., Gagliardini, O., Meyssonnier, J., Zwinger, T., and Ruokolainen, J.: Flow-induced anisotropy in polar ice and related ice-sheet flow modelling, Journal of Non-Newtonian Fluid Mechanics, 134, 33–43, https://doi.org/10.1016/j.jnnfm.2005.11.005, 2006.

Gimbert, F., Nanni, U., Roux, P., Helmstetter, A., Garambois, S., Lecointre, A., Walpersdorf, A., Jourdain, B., Langlais, M., Laarman, O., Lindner, F., Sergeant, A., Vincent, C., and Walter, F.: A Multi-Physics Experiment with a Temporary Dense Seismic Array on the Argentière Glacier, French Alps: The RESOLVE Project, Seismological Research Letters, 92, 1185–1201, https://doi.org/10.1785/0220200280, 2021.

Giordan, D., Dematteis, N., Allasia, P., and Motta, E.: Classification and kinematics of the Planpincieux Glacier break-offs using photographic time-lapse analysis, Journal of Glaciology, 66, 188–202, https://doi.org/10.1017/jog.2019.99, 2020.

Glen, J. W.: The creep of polycrystalline ice, Proceedings of the Royal Society of London. Series A. Mathematical and Physical Sciences, 228, 519–538, 1955.

https://doi.org/10.5194/egusphere-2025-5714
Preprint. Discussion started: 19 December 2025

Grennerat, F., Montagnat, M., Castelnau, O., Vacher, P., Moulinec, H., Suquet, P., and Duval, P.: Experimental characterization of the intragranular strain field in columnar ice during transient creep, Acta Materialia, 60, 3655–3666, https://doi.org/10.1016/j.actamat.2012.03.025, 2012.

Gudmundsson, G. H., Bauder, A., Lüthi, M., Fischer, U. H., and Funk, M.: Estimating rates of basal motion and internal ice deformation from continuous tilt measurements, Annals of Glaciology, 28, 247–252, https://doi.org/10.3189/172756499781821751, 1999.

Gusmeroli, A., Pettit, E. C., Kennedy, J. H., and Ritz, C.: The crystal fabric of ice from full-waveform borehole sonic logging, Journal of Geophysical Research: Earth Surface, 117, https://doi.org/10.1029/2012JF002343, 2012.

Hellmann, S., Kerch, J., Weikusat, I., Bauder, A., Grab, M., Jouvet, G., Schwikowski, M., and Maurer, H.: Crystallographic analysis of temperate ice on Rhonegletscher, Swiss Alps, The Cryosphere, 15, 677–694, https://doi.org/10.5194/tc-15-677-2021, 2021.

Hubbard, B., Roberson, S., Samyn, D., and Merton-Lyn, D.: Digital optical televiewing of ice boreholes, Journal of Glaciology, 54, 823–830, 2008.

Hubbard, B., Christoffersen, P., Doyle, S. H., Chudley, T. R., Schoonman, C. M., Law, R., and Bougamont, M.: Borehole-Based Characterization of Deep Mixed-Mode Crevasses at a Greenlandic Outlet Glacier, AGU Advances, 2, https://doi.org/10.1029/2020av000291, 2021.

Hudleston, P. J.: Structures and fabrics in glacial ice: A review, Journal of Structural Geology, 81, 1–27, https://doi.org/10.1016/j.jsg.2015.09.003, 2015.

Jacka, T. and Budd, W.: Isotropic and Anisotropic Flow Relations for Ice Dynamics, Annals of Glaciology, 12, 81–84, https://doi.org/10.3189/s0260305500006996, 1989.

Jacka, T. and Maccagnan, M.: Ice crystallographic and strain rate changes with strain in compression and extension, Cold Regions Science and Technology, 8, 269–286, https://doi.org/10.1016/0165-232x(84)90058-2, 1984.

Jennings, S. J. A. and Hambrey, M. J.: Structures and Deformation in Glaciers and Ice Sheets, Reviews of Geophysics, 59, https://doi.org/10.1029/2021rg000743, 2021.

Keller, A. and Blatter, H.: Measurement of strain-rate components in a glacier with embedded inclinometers, Journal of Glaciology, 58, 692–698, https://doi.org/10.3189/2012jog11j234, 2012.

Kluskiewicz, D., Waddington, E. D., Anandakrishnan, S., Voigt, D. E., Matsuoka, K., and McCarthy, M. P.: Sonic methods for measuring crystal orientation fabric in ice, and results from the West Antarctic ice sheet (WAIS) Divide, Journal of Glaciology, 63, 603–617, https://doi.org/10.1017/jog.2017.20, 2017.

Lee, I. R., Hawley, R. L., Bernsen, S., Campbell, S. W., Clemens-Sewall, D., Gerbi, C. C., and Hruby, K.: A novel tilt sensor for studying ice deformation: application to streaming ice on Jarvis Glacier, Alaska, Journal of Glaciology, 66, 74–82, https://doi.org/10.1017/jog.2019.84, 2019.

Leet, L. D.: Velocity of Elastic Waves in Granite and Norite, Physics, 4, 375–385, https://doi.org/10.1063/1.1745148, 1933.

Lipenkov, V., Barkov, N., Duval, P., and Pimienta, P.: Crystalline Texture of the 2083 m Ice Core at Vostok Station, Antarctica, Journal of Glaciology, 35, 392–398, https://doi.org/10.3189/s0022143000009321, 1989.

Lliboutry, L. and Duval, P.: Various isotropic and anisotropic ices found in glaciers and polar ice caps and their corresponding rheologies, International Journal of Rock Mechanics and Mining Sciences; Geomechanics Abstracts, 22, 198, https://doi.org/10.1016/0148-9062(85)90267-0, 1985.

https://doi.org/10.5194/egusphere-2025-5714
Preprint. Discussion started: 19 December 2025

Lutz, F., Prior, D. J., Still, H., Bowman, M. H., Boucinhas, B., Craw, L., Fan, S., Kim, D., Mulvaney, R., Thomas, R. E., and Hulbe, C. L.: Ultrasonic and seismic constraints on crystallographic preferred orientations of the Priestley Glacier shear margin, Antarctica, The Cryosphere, 16, 3313–3329, https://doi.org/10.5194/tc-16-3313-2022, 2022.

Lüthi, M., Funk, M., Iken, A., Gogineni, S., and Truffer, M.: Mechanisms of fast flow in Jakobshavn Isbræ, West Greenland: Part III. Measurements of ice deformation, temperature and cross-borehole conductivity in boreholes to the bedrock, Journal of Glaciology, 48, 369–385, https://doi.org/10.3189/172756502781831322, 2002.

Lüthi, M. P., Wasser, D., and Moreau, L.: Calorimetric in-situ determination of ice water content in two Alpine glaciers, https://doi.org/10.5194/egusphere-2025-832, 2025.

Maier, N., Humphrey, N., Harper, J., and Meierbachtol, T.: Sliding dominates slow-flowing margin regions, Greenland Ice Sheet, Science Advances, 5, https://doi.org/10.1126/sciadv.aaw5406, 2019.

Maier, N., Humphrey, N., Meierbachtol, T., and Harper, J.: Deformation motion tracks sliding changes through summer, western Greenland, Journal of Glaciology, 68, 187–196, https://doi.org/10.1017/jog.2021.87, 2021.

Mari, J.-L., Vergniault, C., and Coppens, F.: 3 Acoustic logging, pp. 77–102, EDP Sciences, ISBN 9782759822638, https://doi.org/10.1051/978-2-7598-2263-8.c005, 2020.

Maurel, A., Mercier, J.-F., and Montagnat, M.: Critical investigation of calculation methods for the elastic velocities in anisotropic ice polycrystals, The Cryosphere, 10, 3063–3070, 2016.

Mavko, G. M., Mukerji, T., and Dvorkin, J.: The rock physics handbook, Cambridge Univ. Press, Cambridge [u.a.], 2. ed., repr. edn., ISBN 9780521861366, 2011.

Miles, K. E., Hubbard, B., Miles, E. S., Quincey, D. J., Rowan, A. V., Kirkbride, M., and Hornsey, J.: Continuous borehole optical televiewing reveals variable englacial debris concentrations at Khumbu Glacier, Nepal, Communications Earth amp; Environment, 2, https://doi.org/10.1038/s43247-020-00070-x, 2021.

Montagnat, M., Azuma, N., Dahl-Jensen, D., Eichler, J., Fujita, S., Gillet-Chaulet, F., Kipfstuhl, S., Samyn, D., Svensson, A., and Weikusat, I.: Fabric along the NEEM ice core, Greenland, and its comparison with GRIP and NGRIP ice cores, The Cryosphere, 8, 1129–1138, https://doi.org/10.5194/tc-8-1129-2014, 2014.

Montagnat, M., Chauve, T., Barou, F., Tommasi, A., Beausir, B., and Fressengeas, C.: Analysis of Dynamic Recrystallization of Ice from EBSD Orientation Mapping, Frontiers in Earth Science, 3, https://doi.org/10.3389/feart.2015.00081, 2015.

Monz, M. E., Hudleston, P. J., Prior, D. J., Michels, Z., Fan, S., Negrini, M., Langhorne, P. J., and Qi, C.: Full crystallographic orientation (amp;lt;iamp;gt;camp;lt;/iamp;gt; and amp;lt;iamp;gt;aamp;lt;/iamp;gt; axes) of warm, coarse-grained ice in a shear-dominated setting: a case study, Storglaciären, Sweden, The Cryosphere, 15, 303–324, https://doi.org/10.5194/tc-15-303-2021, 2021.

Moore, P. L.: Deformation of debris-ice mixtures, Reviews of Geophysics, 52, 435–467, https://doi.org/10.1002/2014rg000453, 2014.

Nye, J. F.: The flow law of ice from measurements in glacier tunnels, laboratory experiments and the Jungfraufirn borehole experiment, Proceedings of the Royal Society of London. Series A. Mathematical and Physical Sciences, 219, 477–489, 1953.

Nye, J. F.: The Flow of a Glacier in a Channel of Rectangular, Elliptic or Parabolic Cross-Section, Journal of Glaciology, 5, 661–690, https://doi.org/10.3189/s0022143000018670, 1965.

Qi, C., Goldsby, D. L., and Prior, D. J.: The down-stress transition from cluster to cone fabrics in experimentally deformed ice, Earth and Planetary Science Letters, 471, 136–147, https://doi.org/10.1016/j.epsl.2017.05.008, 2017.

Rabatel, A., Ducasse, E., Millan, R., and Mouginot, J.: Satellite-Derived Annual Glacier Surface Flow Velocity Products for the European Alps, 2015–2021, Data, 8, 66, https://doi.org/10.3390/data8040066, 2023.

https://doi.org/10.5194/egusphere-2025-5714
Preprint. Discussion started: 19 December 2025

Rathmann, N. M., Grinsted, A., Mosegaard, K., Lilien, D. A., Westhoff, J., Hvidberg, C. S., Prior, D. J., Lutz, F., Thomas, R. E., and Dahl-Jensen, D.: Elastic wave propagation in anisotropic polycrystals: inferring physical properties of glacier ice, Proceedings of the Royal Society A: Mathematical, Physical and Engineering Sciences, 478, https://doi.org/10.1098/rspa.2022.0574, 2022.

Rigsby, G. P.: Crystal Orientation in Glacier and in Experimentally Deformed Ice, Journal of Glaciology, 3, 589–606, https://doi.org/10.3189/S0022143000023716, 1960.

Roldán-Blasco, J.-P., Gilbert, A., Piard, L., Gimbert, F., Vincent, C., Gagliardini, O., Togaibekov, A., Walpersdorf, A., and Maier, N.: Creep enhancement and sliding in a temperate, hard-bedded alpine glacier, https://doi.org/10.5194/tc-19-267-2025, 2024.

Ryser, Claudia: Cold ice in an alpine glacier and ice dynamics at the margin of the Greenland Ice Sheet, Ph.D. thesis, https://doi.org/10.3929/ETHZ-B-000093753, 2014.

Saxena, V., Krief, M., and Adam, L.: Stoneley Permeability, pp. 173–204, Elsevier, ISBN 9780128122044, https://doi.org/10.1016/b978-0-12-812204-4.00006-x, 2018.

Schohn, C. M., Iverson, N. R., Zoet, L. K., Fowler, J. R., and Morgan-Witts, N.: Linear-viscous flow of temperate ice, Science, 387, 182–185, https://doi.org/10.1126/science.adp7708, 2025.

Stoll, N., Weikusat, I., Jansen, D., Bons, P., Darányi, K., Westhoff, J., Llorens, M.-G., Wallis, D., Eichler, J., Saruya, T., Homma, T., Drury, M., Wilhelms, F., Kipfstuhl, S., Dahl-Jensen, D., and Kerch, J.: EastGRIP ice core reveals the exceptional evolution of crystallographic preferred orientation throughout the Northeast Greenland Ice Stream, https://doi.org/10.5194/egusphere-2024-2653, 2024.

Thorsteinsson, T., Kipfstuhl, J., and Miller, H.: Textures and fabrics in the GRIP ice core, Journal of Geophysical Research: Oceans, 102, 26 583–26 599, https://doi.org/10.1029/97jc00161, 1997.

Tison, J.-L. and Hubbard, B.: Ice crystallographic evolution at a temperate glacier: Glacier de Tsanfleuron, Switzerland, Geological Society, London, Special Publications, 176, 23–38, https://doi.org/10.1144/gsl.sp.2000.176.01.03, 2000.

Togaibekov, A., Gimbert, F., Gilbert, A., and Walpersdorf, A.: Observing and Modeling Short-Term Changes in Basal Friction During Rain-Induced Speed-Ups on an Alpine Glacier, Geophysical Research Letters, 51, https://doi.org/10.1029/2023gl107999, 2024.

Treverrow, A., Budd, W. F., Jacka, T. H., and Warner, R. C.: The tertiary creep of polycrystalline ice: experimental evidence for stress-dependent levels of strain-rate enhancement, Journal of Glaciology, 58, 301–314, https://doi.org/10.3189/2012jog11j149, 2012.

Vallon, M., Petit, J.-R., and Fabre, B.: Study of an Ice Core to the Bedrock in the Accumulation zone of an Alpine Glacier, Journal of Glaciology, 17, 13–28, https://doi.org/10.3189/s0022143000030677, 1976.

White, J. E.: Underground sound: Application of Seismic Waves, no. 18 in Methods in geochemistry and geophysics, Elsevier, Amsterdam [u.a.], ISBN 0444421394, literaturverz. S. 239 - 245, 1983.

Willis, I., Mair, D., Hubbard, B., Nienow, P., Fischer, U. H., and Hubbard, A.: Seasonal variations in ice deformation and basal motion across the tongue of Haut Glacier d'Arolla, Switzerland, Annals of Glaciology, 36, 157–167, https://doi.org/10.3189/172756403781816455, 2003.

https://doi.org/10.5194/egusphere-2025-5714
Preprint. Discussion started: 19 December 2025

Appendix A: Semblance analysis

Figure A1 presents the semblance analysis performed using equation 3 for the sonic logger receivers located across an open, water-filled crevasse [Fig. A1(a–b)]. The results clearly show a loss of signal coherence for both the P- and Stoneley-waves, with semblance values lower than 0.4. Under these conditions, accurate velocity picking cannot be achieved.

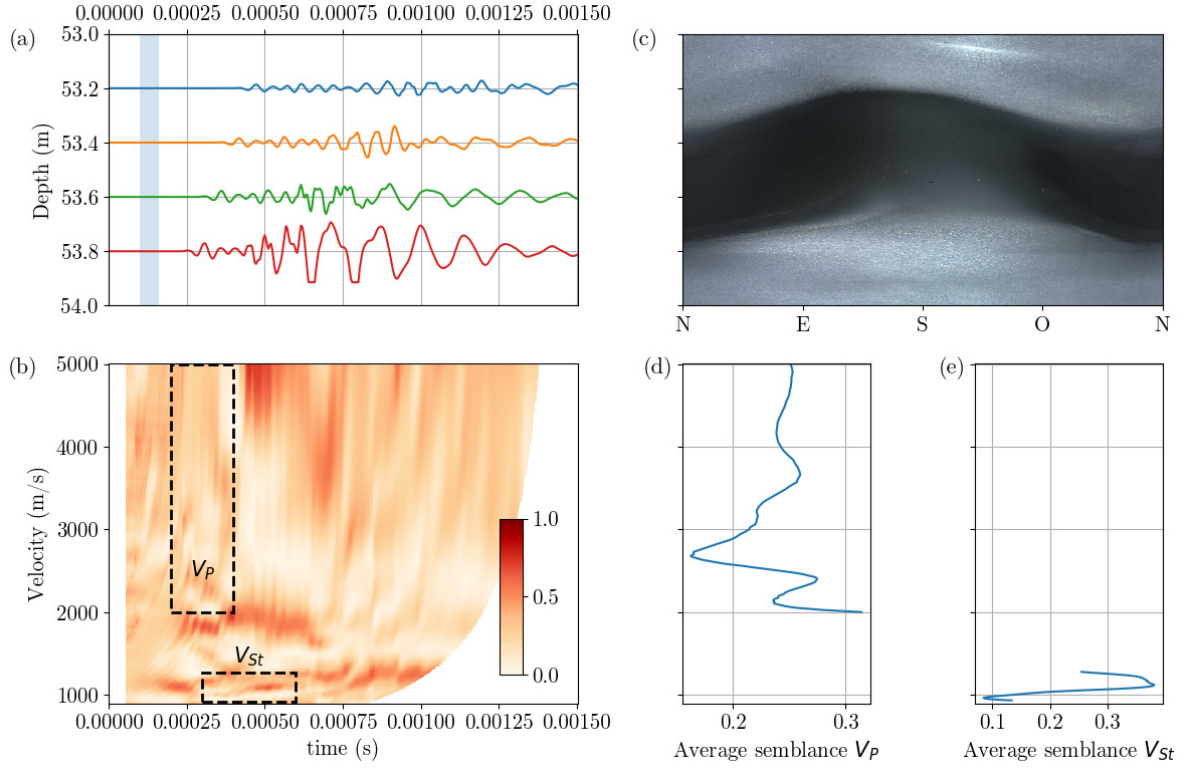

Figure A1. *(a)* Four recorded signals by the sonic logger at 53 m depth. The vertical blue-shaded area shows the length of the wt parameter used in the semblance analysis (Eq. 3). *(b)* The semblance analysis for velocities ranging from 930 to 5000 m s^{-1}. The dashed rectangles show the function range used to determine the P-wave velocity and the Stoneley-wave velocity by taking the maximum of the average semblance over this range *(d)* and *(e)*. *(c)* Optical image recorded by the optical logger at the same depth.

Appendix B: Optical and acoustic loggers

Figure B1 shows two optical logs of the same section of the borehole: one acquired immediately after drilling and the second one day later. The comparison highlights the benefit of allowing time for decantation, which results in a clearer image.

Figures B2, B3, and B4 show additional features observed in the optical and acoustic logs, namely an open crevasse, a dust layer, and several closed crevasses, respectively.

https://doi.org/10.5194/egusphere-2025-5714
Preprint. Discussion started: 19 December 2025

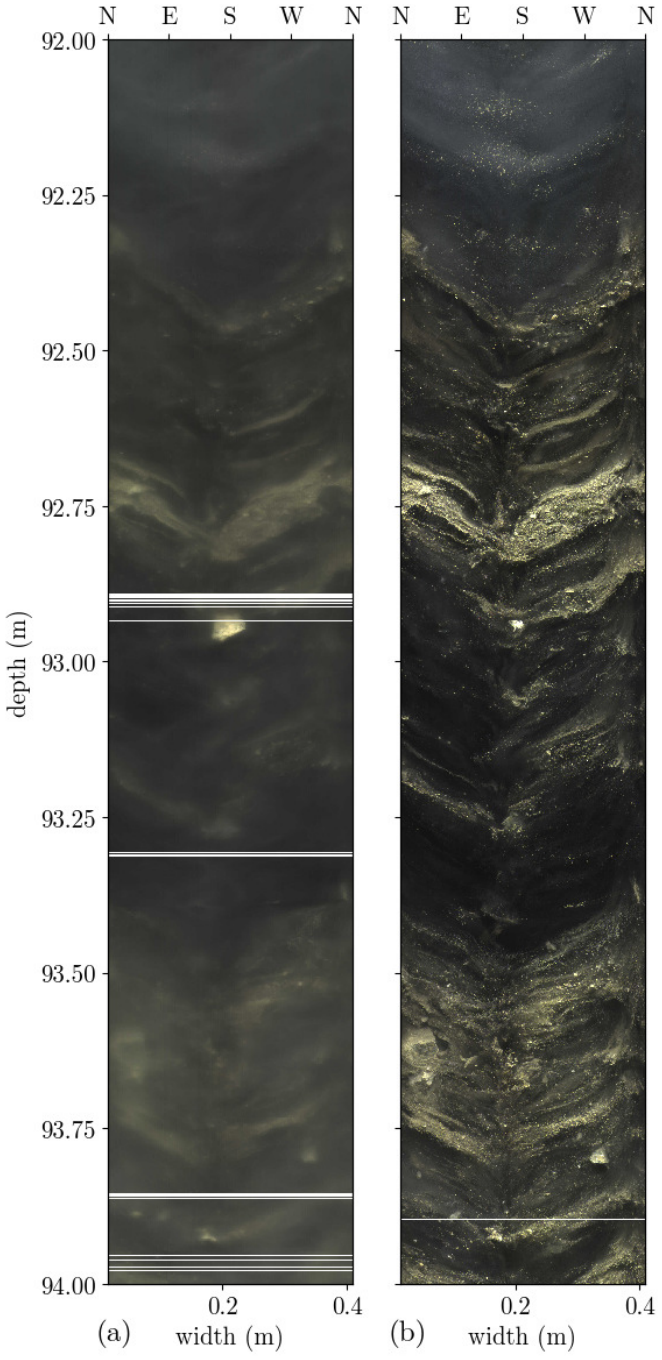

Figure B1. Two optical images of the same borehole lateral surface at a depth of 92 to 94 m. The aspect ratio of the images is preserved, and both are geographically oriented. *(a)* Image taken less than one hour after drilling. *(b)* Image taken 16 h 30 min after panel (a).

https://doi.org/10.5194/egusphere-2025-5714
Preprint. Discussion started: 19 December 2025

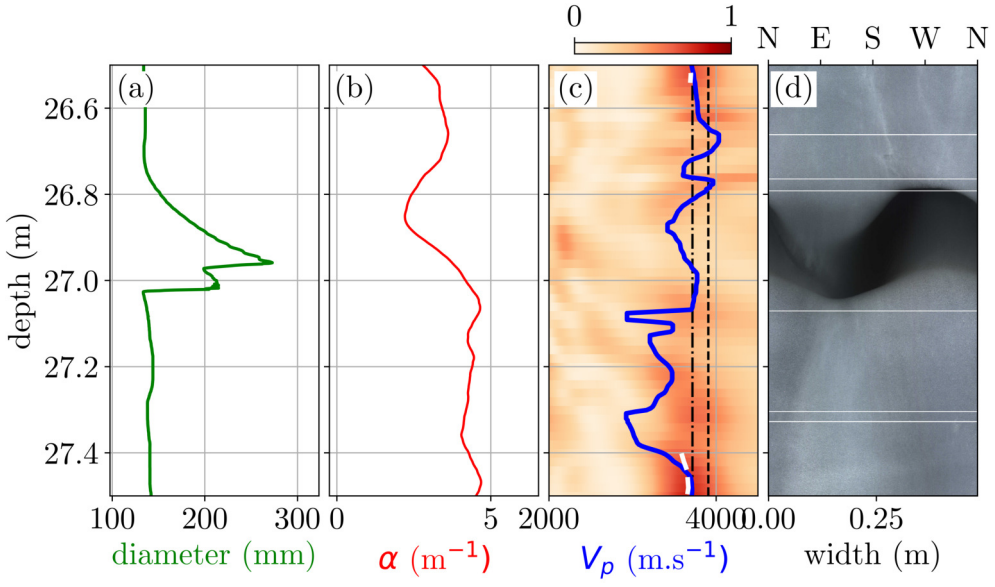

Figure B2. Logs from the borehole probe at 27 m depth. *(a)* Diameter measured by the mechanical caliper. *(b)* Acoustic absorption and *(c)* V_p picking using semblance analysis (white dashed line) or time-of-arrival regression (blue line). *(d)* Oriented optical log horizontally scaled by the average mean diameter given by the caliper.

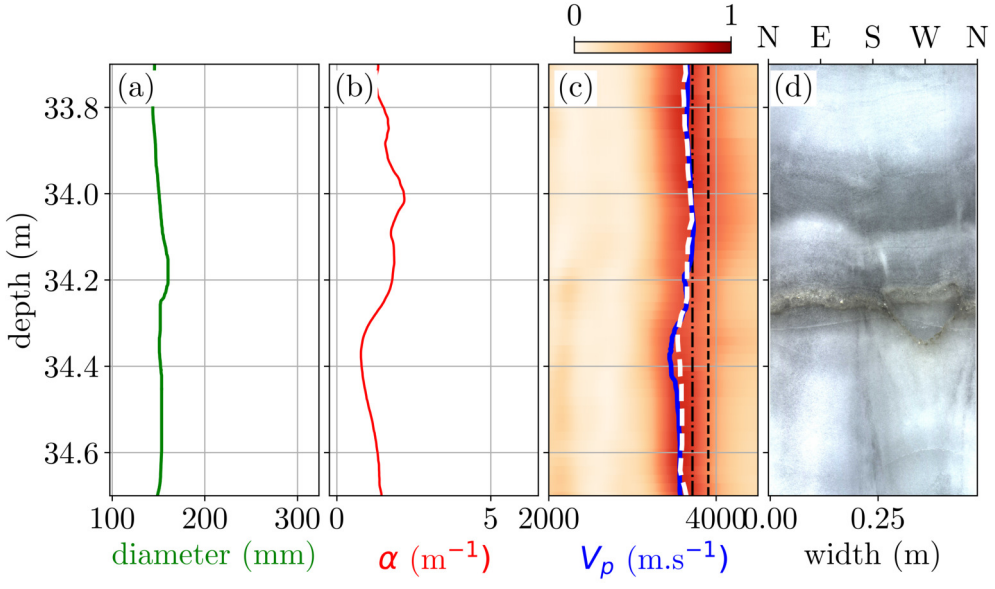

Figure B3. Logs from the borehole probe at 34 m depth. *(a)* Diameter measured by the mechanical caliper. *(b)* Acoustic absorption and *(c)* V_p picking using semblance analysis (white dashed line) or time-of-arrival regression (blue line). *(d)* Oriented optical log horizontally scaled by the average mean diameter given by the caliper.

https://doi.org/10.5194/egusphere-2025-5714
Preprint. Discussion started: 19 December 2025

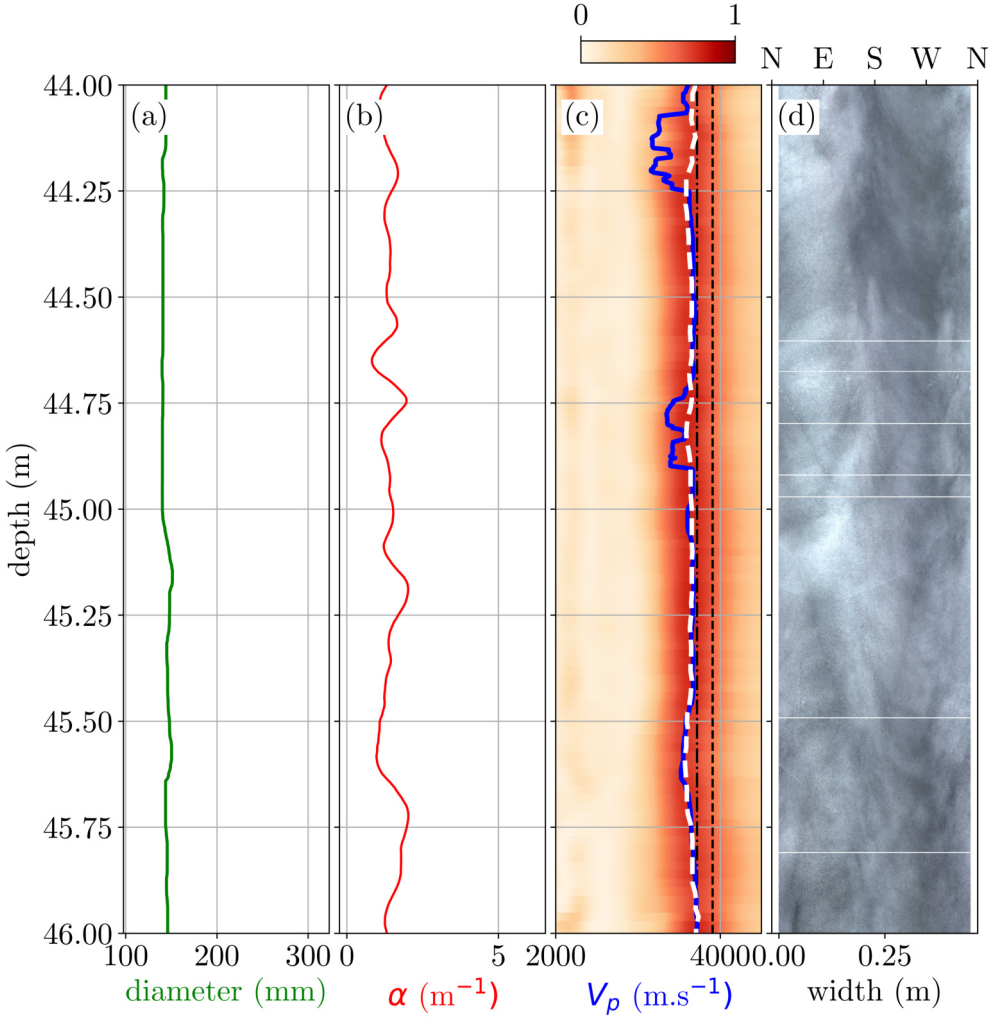

Figure B4. Logs from the borehole probe at 45 m depth. *(a)* Diameter measured by the mechanical caliper. *(b)* Acoustic absorption and *(c)* V_p picking using semblance analysis (white dashed line) or time-of-arrival regression (blue line). *(d)* Oriented optical log horizontally scaled by the average mean diameter given by the caliper.

https://doi.org/10.5194/egusphere-2025-5714
Preprint. Discussion started: 19 December 2025

Appendix C: Caliper measurement

The diameter profile measured by a mechanical caliper during crevasse crossings is influenced by the design and geometry of the measurement system. Figure C1 illustrates the three key steps that explain the typical profiles observed in Figs. B2 and 5.

The caliper was moved from bottom to top, initially measuring the borehole diameter (Fig. C1(a)). When the caliper arm tip reaches point A (Fig. C1(b)), the measured diameter shows a discontinuity. This is controlled either by contact at point B on the caliper arms or, in the case of a large crevasse, by the mechanical limit of the caliper extension.

As the caliper continues to be pulled upward, point B slides along the arm until it reaches the tip. During this process, the measured angle Φ decreases, following the relation $\Phi = \arctan\left(\frac{r}{z}\right)$, where r is the borehole radius and z is the depth of the measurement (Fig. C1(c)).

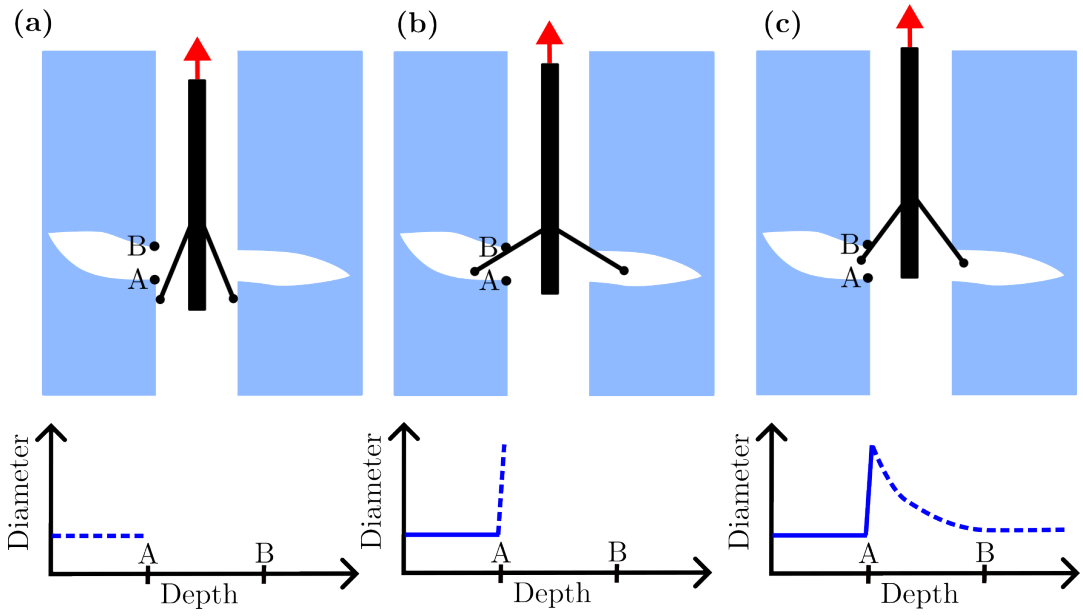

Figure C1. Schematic illustration of the mechanical caliper probe during the crossing of an open crevasse.

Figure C2 shows the log of the caliper from 55 to 90 m depth exhibiting a negative trend of -0.09 mm.m^{-1}.

https://doi.org/10.5194/egusphere-2025-5714
Preprint. Discussion started: 19 December 2025

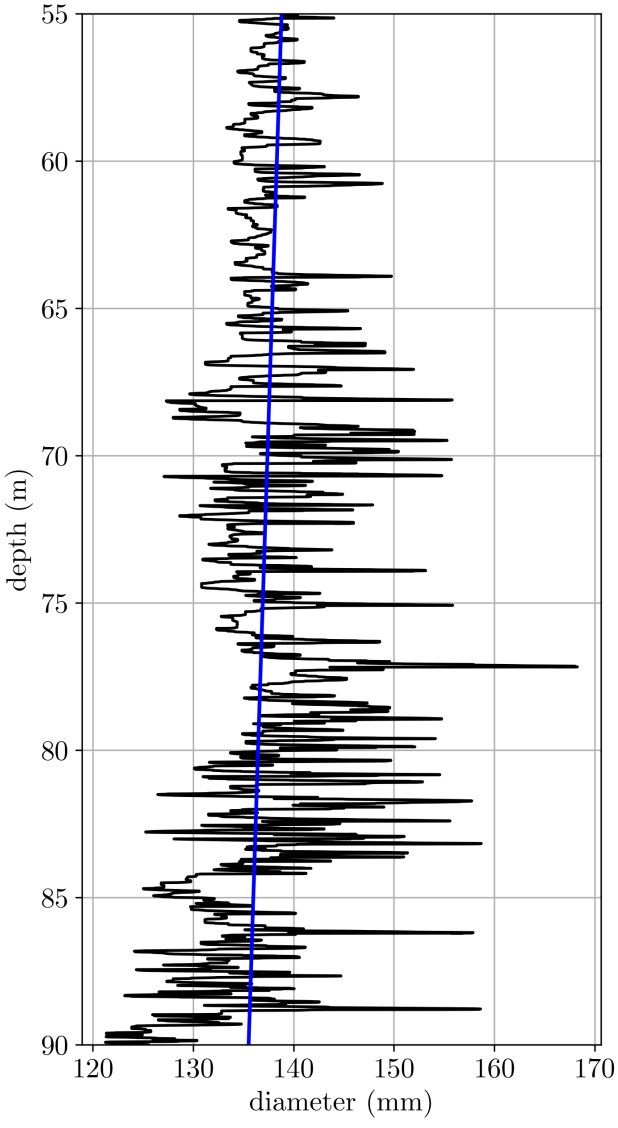

Figure C2. Diameter of the borehole from 55 to 90 m depth measured by the caliper. The blue line shows the linear regression over this section, revealing a negative trend of -0.09 mm.m^{-1}.

https://doi.org/10.5194/egusphere-2025-5714
Preprint. Discussion started: 19 December 2025

Appendix D: Inclinometer data

Figure D1 shows the time series recorded by each sensor along the inclinometer chain. The dashed area indicates the period during which the data were excluded from the statistics presented in Fig. 10, as the mechanical coupling with the ice was assumed to be insufficient.

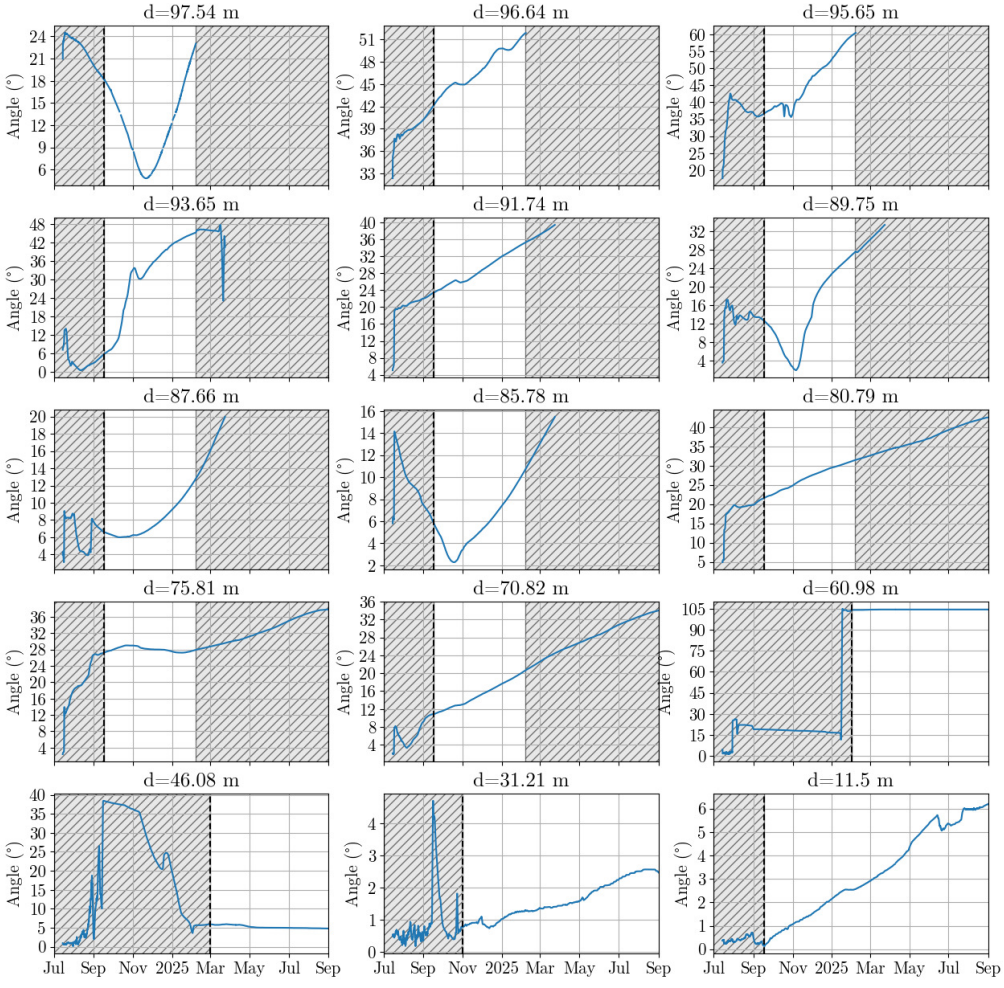

Figure D1. Raw angle data from the inclinometers in the *RBT_H* borehole. The black dashed line indicates the date at which all the inclinometers are considered to be mechanically coupled with the surrounding ice.

https://doi.org/10.5194/egusphere-2025-5714
Preprint. Discussion started: 19 December 2025

Appendix E: Shape factor estimation

Figure E1 shows a cross section of the glacier, transverse to the flow direction at the borehole location. It is used to estimate the glacier aspect ratio W, which is related to the shape factor f following Nye (1965). The glacier width transverse to flow is approximately twice the maximum depth, giving $W = 1$, which corresponds to $f \approx 0.5$ in Nye (1965) tabulation.

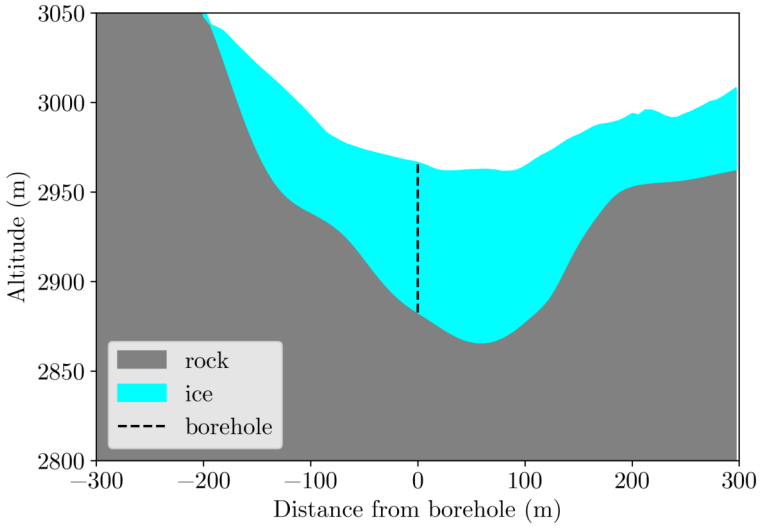

Figure E1. Cross-section of the glacier passing through the borehole and normal to the flow direction.